1 Mitochondrial cyclophilin D promotes disease tolerance by licensing NK cell development

2 and IL-22 production against influenza virus

3

4 Jeffrey Downey[1], Haley E. Randolph[2], Erwan Pernet[1], Kim A. Tran[1], Shabaana A. Khader[3], Irah

5 L. King[1], Luis B. Barreiro[2,4] and Maziar Divangahi[1*]

6

7 1. Department of Medicine, Department of Pathology, Department of Microbiology & Immunology,

8   McGill University Health Centre, McGill International TB Centre, Meakins-Christie Laboratories,

9   McGill University, 1001 Decarie Boulevard, Montreal, Quebec, H4A 3J1, Canada.

10 2. Genetics, Genomics, and Systems Biology, University of Chicago, Chicago, IL, USA.

11 3. Department of Pathology and Immunology, Department of Molecular Microbiology, Washington

12   University School of Medicine, St. Louis, MO, United States.

13 4. Section of Genetic Medicine, Department of Medicine, University of Chicago, Chicago, IL, USA.

14

15

16

17 Corresponding Author:

18 Maziar Divangahi, Ph.D.

19 Associate Professor of Medicine

20 RI-MUHC, Centre for Translational Biology

21 Meakins-Christie Laboratories

22 1001 Decarie Blvd,

23 Block E (EM3.2248)

24 Montreal, Quebec H4A 3J1

25
26 Tel: (514) 934-1934 Ext. 76431
27 e-mail: maziar.divangahi@mcgill.ca

28   **ABSTRACT**

29   Immunity to infectious disease involves a combination of host resistance, which eliminates the

30   pathogen, and disease tolerance, which limits tissue damage. While the severity of most pulmonary

31   viral infections, including influenza A virus (IAV), is linked to excessive inflammation, our

32   mechanistic understanding of this observation remains largely unknown. Here we show that

33   mitochondrial cyclophilin D (CypD) protects against IAV infection via disease tolerance. Mice

34   deficient in CypD (*CypD*$^{-/-}$ mice) are significantly more susceptible to IAV infection despite

35   comparable antiviral immunity. Instead, this susceptibility resulted from damage to the lung

36   epithelial barrier caused by a significant reduction of IL-22 production by conventional NK cells

37   in IAV-infected *CypD*$^{-/-}$ mice. Transcriptomic and functional data revealed that the compromised

38   IL-22 production by NK cells resulted from dysregulated lymphopoiesis, stemming from increased

39   cell death in NK cell progenitors, as well as the generation of immature NK cells that exhibited

40   altered mitochondrial metabolism. Importantly, following IAV infection, administration of

41   recombinant IL-22 abrogated pulmonary damage and enhanced survival of *CypD*$^{-/-}$ mice.

42   Collectively, these results demonstrate a key role for CypD in NK cell-mediated disease tolerance.

43

44

45

46

47   **KEYWORDS:** Influenza, Disease Tolerance, Cyclophilin D, IL-22, NK cells, Lymphopoiesis

48

49

50

INTRODUCTION:

In response to any given infection, host resistance mechanisms are involved in preventing pathogen invasion or replication. These resistance mechanisms are a critical component of host defense to infection, yet they come with a considerable inflammatory cost that paradoxically threatens host fitness through excessive immunopathology. Thus, mechanisms of disease tolerance are required to mitigate tissue damage, restore organ function and counter the cost of anti-microbial inflammation (*1-4*).

Influenza A viruses (IAV) cause consistent and recurrent respiratory infections, responsible for approximately half a million deaths per annum globally, while also causing unpredictable and devastating pandemics. Severe and fatal IAV infections are more often triggered by a "cytokine storm" that contributes to a break in disease tolerance—characterized by destruction of the pulmonary epithelial/endothelial barrier and respiratory insufficiency—rather than ineffective host resistance (*5-7*). On the other hand, 16% of IAV infections are estimated to be asymptomatic (*8*) and similar observations have been made clinically during the COVID-19 pandemic. Like influenza, deaths due to COVID-19 seem to be more often associated with a loss of disease tolerance (*9, 10*), suggesting that in certain individuals these mechanisms are sufficient to avoid severe disease manifestation. Thus, understanding disease tolerance responses against a variety of acute respiratory infections may uncover targetable pathways for novel immunotherapies.

IAV infections are short-lived and usually self-resolving within approximately 7-10 days, though inflammation can persist for weeks after infection. The early inflammatory response is marked by an influx of innate leukocytes into the infected lung and airways. While inflammatory monocyte-derived cells play important roles in host resistance and priming of the adaptive immune

74   response (*11-13*), they can jeopardize survival through immunopathology (*14, 15*).

75   Mechanistically, our group recently highlighted the importance of the bioactive lipid leukotriene

76   B_4 (LTB$_4$) in inhibiting *in situ* proliferation of inflammatory monocyte-derived macrophages

77   (IMM) to conserve pulmonary epithelial integrity (*16*). Equally, reduction of extracellular matrix

78   (ECM) turnover during IAV infection, by inhibiting lung metalloprotease activity, protected mice

79   by conserving epithelial structure (*17*). Thus, maintenance of the pulmonary architecture and

80   physiology is an essential component of host defense to IAV infection.

81   In addition to myeloid cells, innate lymphoid cells (ILCs), such as natural killer (NK) cells,

82   accumulate in the lung shortly upon infection, beginning as early as 2 days post-infection (*18*). NK

83   cells express a variety of activating and inhibitory receptors that perform diverse context- and

84   tissue-specific functions, including well-described roles in the killing of virally-infected cells in a

85   non-MHC-restricted manner through the production of IFN-γ and expression of perforin and

86   granzymes (*19*). In the context of IAV infection, NK cells contribute to host resistance by

87   recognizing sialylated hemagglutinin (HA) proteins (*20, 21*) on the surface of IAV-infected cells

88   to facilitate lysis (*22-24*). Beyond their cytotoxic role in host resistance, NK cells are equally

89   critical in disease tolerance by secreting the epithelium-protective cytokine IL-22 (*25*). IL-22 is a

90   member of the IL-10 family of cytokines that maintains mucosal barriers by inducing survival and

91   proliferation of epithelial cells. Although several cell types are capable of producing IL-22—

92   including NKT cells, γδ T-cells, ILC3s and αβ T-cells (*26, 27*)—conventional NK cells have been

93   suggested to be the major source following IAV infection (*28*), particularly at later time-points

94   (*29*). Consistently, *Il22*^{-/-} mice exhibit enhanced epithelial damage and pulmonary pathology in

95   response to IAV (*26, 29, 30*). However, our understanding of the mechanisms involved in the

96   production of IL-22 by NK cells in this setting is incomplete.

97   Mitochondrial Cyclophilin D (CypD), encoded in the nucleus by the *Peptidyl-prolyl*

98   *isomerase F* (*Ppif*) gene, is a member of the cyclophilin family of isomerases that resides within

99   the mitochondrial matrix. CypD is well-known as an essential modulator of the mitochondrial

100   permeability transition pore (MPTP) which is required for the induction of necrosis (*31-33*). Given

101   the regulatory role of CypD in macrophage necrosis (*32, 33*) and the importance of conserved

102   macrophage viability/function in immunity to IAV (*34-36*), we initially hypothesized that the loss

103   of CypD-mediated necrosis would enhance macrophage viability and, thus, protection to IAV

104   infection. Surprisingly, CypD-deficient mice were highly susceptible to IAV infection without

105   aberrations in host resistance mechanisms or leukocyte necrosis. A lack of IL-22 production by

106   conventional NK cells in the infected airways of $CypD^{-/-}$ mice was the major cause of

107   susceptibility, as exogenous reconstitution of $CypD^{-/-}$ mice with IL-22, or transfer of wild type

108   (WT), but not CypD-deficient, NK cells into $Il22^{-/-}$ mice significantly improved disease tolerance.

109   RNA-seq of purified NK cells from IAV-infected mice revealed a unique transcriptome in CypD-

110   deficient NK cells, marked by an immature profile (*37*). We found that CypD promotes NK cell

111   responses at two levels: (1) by preventing cell death of NK cell progenitors in the bone marrow

112   to facilitate NK cell hematopoiesis; and (2) by regulating peripheral NK cell metabolism, which is

113   required for the conversion of immature to mature NK cells (*38*). Collectively, our findings

114   highlight an essential role for CypD in NK cell-mediated disease tolerance to acute IAV infection.

115

116

117   **RESULTS:**

118

119   **CypD is required for host defense to influenza A virus infection by promoting disease**

120   **tolerance**

121   Given the requirement of CypD in necrosis (*31, 32*) and the relationship between influenza

122   A virus (IAV) pathogenesis and cell death (*34*), we postulated that *CypD$^{-/-}$* mice are more

123   resistance to IAV infection. We first infected WT and *CypD$^{-/-}$* mice with an LD$_{50}$ (90 PFU) dose

124   of PR8 IAV. *CypD$^{-/-}$* mice were highly susceptible to IAV infection, exhibiting increased mortality

125   (**Fig. 1A**) and morbidity (**Fig. 1B**). To delineate the cause of mortality, we hereafter used a

126   sublethal (50 PFU) dose of IAV. Interestingly, the enhanced susceptibility of *CypD$^{-/-}$* mice was not

127   due to differences in pulmonary necrosis (**Fig. S1A**) or host resistance, as *CypD$^{-/-}$* mice had similar

128   pulmonary viral loads (**Fig. 1C**) and levels of active type I IFN (IFN-I) in the lung (**Fig. 1D-E;**

129   **Fig. S1B-C**). We next hypothesized that the susceptibility of *CypD$^{-/-}$* mice was linked to impaired

130   disease tolerance responses, leading to increased lung tissue damage and pulmonary inflammation.

131   Following IAV infection, CypD-deficient mice exhibited enhanced pulmonary edema (**Fig. 1F**)

132   and barrier damage, as there was significant increase in protein and erythrocyte influx into the

133   BAL (**Fig. 1G-H; Fig. S1D**). Intranasal delivery of a fluorescently-labelled dextran molecule into

134   infected mice further demonstrated a significant increase in lung epithelial/endothelial damage of

135   *CypD$^{-/-}$* mice through a collective loss of fluorescence in the lung over time (**Fig. 1I**). Both flow

136   cytometry and H&E staining showed that this increased pulmonary damage was associated with

137   elevated inflammatory cells in the parenchyma and airways of *CypD$^{-/-}$* lungs (**Fig. 1J-L**) beginning

138   at 7 days post-infection, which coincided with the onset of enhanced tissue damage in these mice.

139   Using Masson's Trichrome stain, we equally observed enhanced collagen deposition and fibrosis

140   in the lungs of $CypD^{-/-}$ mice (**Fig. 1M-N**). Taken together, these data show that CypD is required

141   in immunity to IAV by regulating disease tolerance, rather than host resistance.

Immune, not stromal, cells are responsible for the susceptibility of $CypD^{-/-}$ mice to IAV

143   Mechanisms of disease tolerance can be mediated by either structural or hematopoietic

144   compartments (*1, 3, 39*). To delineate which cellular compartment was primarily responsible for

145   the increased tissue damage in $CypD^{-/-}$ mice, we generated bone marrow chimeric mice, where the

146   hematopoietic compartment of lethally irradiated CD45.1 WT mice was reconstituted with CypD-

147   deficient (CD45.2) ($CypD^{-/-}$ → WT) bone marrow (BM) and vice versa (WT→ $CypD^{-/-}$). After 10-

148   12 weeks, reconstitution efficiency was greater than 92% (**Fig. S2A**). For further analysis, we

149   chose day 7 post-IAV infection to match the peak lung damage and initial mortality of the CypD-

150   deficient mice (**Fig. 1**). Chimeric mice reconstituted with $CypD^{-/-}$ BM cells ($CypD^{-/-}$ → WT)

151   showed a statistically significant increase in erythrocytes in the BAL and enhanced pulmonary

152   inflammation and collagen deposition when compared to WT (**Fig. 2A-D; Fig. S2B**). These results

153   indicate that the reduced disease tolerance in CypD-deficient mice is predominately mediated by

154   the hematopoietic compartment.

155   To elucidate which cell(s) of the hematopoietic compartment is/are responsible for the

156   increased lung damage, we extensively phenotyped innate immune cells by flow cytometry (**full**

157   **gating strategy Fig. S1 E-F**) at various time points post-IAV infection in the lung parenchyma

158   and airways. We and others have previously shown that elevated levels of IMM and neutrophils

159   can compromise disease tolerance during IAV infection (*11, 16*). However, the kinetics of IMM

160   and neutrophils in the BAL showed no significant differences in frequencies or numbers between

161   WT and $CypD^{-/-}$ mice (**Fig. 2E-F**) and even showed a trending decrease in $CypD^{-/-}$ mice.

162   Interestingly, we found that the kinetics of NK cell accumulation in the airways differed between

163   CypD-deficient and WT mice, with a significant reduction in the frequency of NK cells at day 7

164   post-IAV infection in *CypD$^{-/-}$* mice, which aligned with the pulmonary damage (**Fig. 2G**). No

165   differences in any of the cell populations assessed were observed in the lung parenchyma (**Fig.**

166   **S2C-E**), hinting at the importance of spatial lung immunity (i.e. parenchyma versus airways)

167   during IAV infection.

168   **CypD-deficient NK cells are phenotypically immature**

169   NK cells are required for protection against IAV by regulating both host resistance and disease

170   tolerance (*23, 29*). Correspondingly, a recent study suggested that altered kinetics of NK cells may

171   underlie individual susceptibility to IAV, without affecting early viral loads (*40*). Thus, we next

172   sought to further interrogate the role of NK cells in the susceptibility of CypD-deficient mice to

173   IAV. NKp46/IAV HA interactions elicit cell lysis via perforin and granzyme to kill virally infected

174   cells (*21, 23*). However, CypD-deficient and WT NK cells expressed similar levels of perforin and

175   granzyme B (**Fig. 2H**), suggesting the lytic capacity of CypD-deficient NK cells was intact, as

176   predicted given the similar viral loads in these mice. The maturation and accumulation of effector

177   functions in NK cells is known to be dependent on downregulation of CD27 and upregulation of

178   CD11b, which gives rise to four distinct populations of NK cells (CD27$^-$ CD11b$^-$, CD27$^+$ CD11b$^-$

179   , CD27$^+$ CD11b$^+$, CD27$^-$ CD11b$^+$) (*37, 41, 42*). Unbiased single cell analysis has confirmed the

180   existence of these populations and their importance in determining effector function of NK cells

181   in mice (*43*). Intriguingly, *CypD$^{-/-}$* NK cells exhibited a significantly higher frequency and number

182   of immature (CD27$^+$ CD11b$^-$) cells compared to fully mature (CD27$^-$ CD11b$^+$) cells in the BAL

183   (**Fig. 2I-J**), but not the lung (**Fig. S2F-G**) at day 7 post-IAV infection. Similar results as in the

184   BAL were obtained in splenic NK cells at day 5 post-IAV infection (**Fig. S2H**). Collectively, our

185   results show that CypD-deficient mice have reduced accumulation of mature NK cells in the

186   airways at the peak of IAV-induced immunopathology.

187   **_CypD^{-/-}_ NK cells have a unique transcriptional profile and metabolic program following IAV**

188   **infection**

189   As NK cell kinetics and maturity differed between WT and _CypD^{-/-}_ mice following IAV

190   infection, we next asked whether _CypD_ was expressed in NK cells. To investigate this, we purified

191   NK cells from WT and CypD-deficient spleens and found significant expression of _CypD_ in WT,

192   but not _CypD^{-/-}_ cells, both at steady-state and upon infection (**Fig. S3A**), which aligned with data

193   publicly available from ImmGen (*44*). We then performed bulk RNA-seq on WT and CypD-

194   deficient splenic NK cells isolated at day 5 post-IAV infection (**Table S1**). We chose day 5 post-

195   infection, as splenic _CypD^{-/-}_ NK cells already exhibited an immature effector state when compared

196   to WT (**Fig. S2H**). Principal component analysis (PCA) on the splenic WT and _CypD^{-/-}_ NK cell

197   expression data revealed a strong signature of IAV infection, with non-infected and IAV-infected

198   samples separating on PC1, which explains 56.3% of the variance in the dataset (**Fig. S3B**). Within

199   the IAV-infected samples, we found 315 genes for which expression patterns significantly differed

200   ($|logFC| > 0.5$, FDR < 0.10) between WT and _CypD^{-/-}_ mice (**Fig. 3A; Table S2**), including _Ppif_ in

201   line with our qPCR data (**Fig. S3A**). Gene ontology (GO) enrichment analysis revealed that genes

202   showing significantly higher expression in the WT mice (n = 146) were enriched for pathways

203   related to activation of the immune response (FDR = $4.3x10^{-4}$), phagocytosis (FDR = $5.3x10^{-5}$),

204   wound healing (FDR = $4.1x10^{-4}$), and blood coagulation (FDR = $5.3x10^{-4}$) (**Fig. 3B; Table S3**),

205   while genes more highly expressed in the _CypD^{-/-}_ mice (n = 169) were enriched for oxidative

206   phosphorylation (OXPHOS) (FDR = $2.5x10^{-3}$), T cell mediated toxicity (FDR = $3.2x10^{-3}$),

207   porphyrin-containing compound metabolic processes (FDR = $5.1x10^{-3}$), and peroxidase activity

208   (FDR = 1.5×10^{-4}) (**Fig. 3C; Table S3**). In line with our observation that $CypD^{-/-}$ mice display

209   significantly more immature ($CD27^+CD11b^-$) and fewer fully mature ($CD27^-$ $CD11b^+$) NK cells,

210   we found that genes previously associated with elevated expression in fully mature and

211   intermediate-mature ($CD27^+$ $CD11b^+$) NK cells (Chiossone et al., 2009) were significantly

212   enriched among genes showing higher expression in WT compared to $CypD^{-/-}$ mice (**Fig. S3C**)

213   and that key genes driving these enrichments exhibited lower expression in $CypD^{-/-}$ mice (**Fig.**

214   **3D**).

215   Gene set enrichment analysis (GSEA) using the Molecular Signatures Database hallmark

216   gene sets (*45*) highlighted a divergence in multiple metabolic and signaling pathways between WT

217   and $CypD^{-/-}$ mice, including an enrichment for Wnt/β-catenin signaling among genes more highly-

218   expressed in WT mice (FDR = 0.024) (**Fig. 3E; Table S3**), and enrichments for mTORC1

219   signaling (FDR = 3.3×10^{-4}) and OXPHOS (FDR = 1.7×10^{-4}) among genes more highly-expressed

220   in $CypD^{-/-}$ mice (**Fig. 3F-G; Table S3**), suggesting a distinct metabolic program in CypD-deficient

221   NK cells. Concordant with our enrichment analyses, the average expression of genes belonging to

222   the Wnt/β-catenin signaling pathway was significantly higher in WT compared to $CypD^{-/-}$ mice

223   (**Fig. 3H**, t-test, p = 4.2×10^{-3}), while for the OXPHOS and mTORC1 signaling pathways, we

224   observed a trend toward higher expression in the $CypD^{-/-}$ compared to WT mice (**Fig. S3D-E**, t-

225   test, p = 0.06 and p = 0.24, respectively).

226   The RNA-seq results underscored an immature effector transcriptome in CypD-deficient

227   NK cells, including decreased expression of the Wnt/β-catenin signaling pathway that has been

228   shown to be a critical in the progression to mature $CD11b^+$ NK cells (*46*), as well as an upregulation

229   of OXPHOS and mTORC1 signaling, both of which have been implicated in immature effector

230   states and impaired activation of NK cells (*38, 47, 48*). CypD is equally known to regulate ATP

231   synthase and OXPHOS through incompletely understood mechanisms (*49*). To see whether an

232   enhanced OXPHOS pathway expression led to elevated mitochondrial respiration in CypD-

233   deficient NK cells, we purified splenic NK cells and subjected them to the Seahorse assay. At

234   steady-state, we detected no differences in OXPHOS in WT and *CypD$^{-/-}$* NK cells (**Fig. S3F-I**).

235   However, over the course of infection, we observed a significant increase in basal metabolic rate,

236   maximal respiration and spare respiratory capacity in *CypD$^{-/-}$* NK cells compared to WT (**Fig. 3I-**

237   **P**). We also found an increase in healthy respiring and disrupted mitochondria in CypD-deficient

238   NK cells at day 3 post-infection (**Fig. 3Q-S**), as well as enhanced mitochondrial ROS production

239   (**Fig. 3T**), suggesting the elevated OXPHOS contributes to mitochondrial dysregulation. Taken

240   together, RNA-seq, flow cytometry and functional data indicate that CypD within NK cells enables

241   their maturation and regulates cellular metabolism.

242   ***CypD* expression in NK cells promotes transcriptional pathways involved in wound healing**

243   **and hemostasis**

244   We next sought to dissect the transcriptional differences in functional immune-related

245   pathways between WT and CypD-deficient NK cells following IAV infection. Numerous killer

246   cell lectin-like receptor genes (*Klr*) were significantly differentially-expressed between NK cells

247   of WT and *CypD$^{-/-}$* mice post-infection (**Fig. 3A**), including *Klri2*, *Klr8*, *Klra17*, and *Klra5*, among

248   others, suggesting that the inhibitory and activating capacity of these NK cells may differ, which

249   in turn may alter their functional capabilities. Indeed, the transcriptional immune response

250   signatures of IAV-infected WT and *CypD$^{-/-}$* NK cells were distinct from one another: genes

251   displaying significantly higher expression in *CypD$^{-/-}$* NK cells were enriched for antigen

252   processing (FDR = 7.8×10^{-3}) and T cell mediated cytotoxicity (FDR = 3.2×10^{-3}) pathways (**Fig.**

253   **4A; Table S3**), whereas genes more highly-expressed in WT NK cells were enriched for effector

254   functions related to phagocytosis and engulfment (FDR = 1.1×10^{-3}) and complement-dependent

255   cytotoxicity (FDR = 8.0×10^{-4}) (**Fig. 4B; Table S3**). Notably, among genes more highly-expressed

256   in WT NK cells, we also identified significant enrichments for multiple pathways involved in

257   cytokine secretion, including IL-2 production (FDR = 8.1×10^{-3}), IL-10 secretion (FDR = 1.2×10^{-3})

258   ^{3}) and production (FDR = 5.6×10^{-3}), negative regulation of IL-13 secretion (FDR = 6.8×10^{-4}), and

259   chemokine secretion (FDR = 1.8×10^{-3}), (**Fig. 4B; Table S3**), suggesting that $CypD^{-/-}$ NK cells

260   display impaired anti-inflammatory cytokine production compared to WT NK cells. Finally, in

261   agreement with our previous observation that the WT NK cell transcriptome was enriched for

262   pathways involved in blood coagulation (**Fig. 3B**) and that CypD-deficient mice had enhanced

263   hemorrhaging (**Fig. 1H; Fig. S1D**), genes upregulated in WT compared to $CypD^{-/-}$ cells were

264   enriched for hemostasis (FDR = 5.5×10^{-4}). Moreover, negative regulation of fibroblast growth

265   factor production (FDR = 1.5×10^{-3}) was enriched in WT NK cells, which might explain the reduced

266   fibrosis in WT lungs following IAV infection (**Fig. 1M-N**). Interestingly, one gene significantly

267   upregulated in this pathway in WT cells, $Cd59a$, has previously been shown to mediate protection

268   against IAV, in part, via inhibiting pulmonary hemorrhaging and fibrosis in the lung (*50*),

269   suggesting a complementary role of CypD. Finally, genes showing significantly higher expression

270   in WT mice were more likely to be found in the tissue repair gene set (Yanai et al., 2016) than

271   expected by chance (WT p = 0.009), while no such enrichment was observed among genes more

272   highly-expressed in $CypD^{-/-}$ mice ($CypD^{-/-}$ p = 0.798) (**Fig. 4C**), further underscoring the role of

273   CypD in mediating disease tolerance.

274

275

CypD promotes NK cell hematopoiesis within bone marrow progenitors to generate mature peripheral NK cells

Considering the functional role of CypD in cell death, the lack of developmentally mature NK cells in the airways of *CypD$^{-/-}$* mice following IAV infection might be due to perturbations in local proliferation and/or cell death. To investigate these possibilities, we analyzed markers of proliferation (Ki67) and cell death (active caspase 3) by flow cytometry within NK cells in the BAL and found no differences (**Fig. 5A-B**). In addition to proliferation and cell death, aberrant recruitment or chemotaxis into the airways could explain the reduced number of mature NK cells in CypD-deficient mice. CCR2 expression on NK cells is known to specifically facilitate migration of NK cells into the airways, without affecting extravasation into the lung, which is instead mediated by CX3CR3 (*18, 51*). However, the frequency of CCR2$^+$ NK cells was indistinguishable between WT and *CypD$^{-/-}$* mice in the BAL, lung and blood (**Fig. 5C; Fig. S4A-B**), confirming CCR2-mediated migration of NK cells into the airways is not dependent on CypD expression.

Although continual on-demand egress of NK cells from the BM into the blood to supply peripheral tissues is well-described, it is now known that an additional population of long-lived tissue-resident NK cells exists in several peripheral tissues that can be differentiated by expression of CD49a rather than CD49b (*52*). This population is most prevalent in the uterus, liver and skin, but can be found in a variety of other sites, including the lung (*53*). To see whether this population of tissue-resident NK cells was altered in our model, we investigated expression of CD49a versus CD49b on the surface of NK cells from WT and *CypD$^{-/-}$* mice. The vast majority of NK cells from the BAL and lungs of both groups of mice were CD49b$^+$ CD49a$^-$, indicative of a predominantly blood-derived population, and this frequency was the same between both groups (**Fig. 5D; Fig. S4C**). Thus, differences in blood-derived versus resident NK cells is not the reason for the altered

13

299   accumulation and effector states observed in $CypD^{-/-}$ mice. Interestingly, the frequency of NK cells

300   in the peripheral blood was decreased in CypD-deficient mice (**Fig. 5E**), and there were less fully

301   mature $CD27^-$ $CD11b^+$ cells at day 5 post-infection, but not at other time points (**Fig. 5F-G; Fig.**

302   **S4D-E**), suggesting NK cell recruitment was altered in $CypD^{-/-}$ mice.

303   The reduction of fully mature NK cells in the blood and peripheral tissue led us to speculate

304   that there was a defect in the generation of NK cells in the BM of $CypD^{-/-}$ mice. NK cell generation

305   occurs through a stepwise progression of progenitors, ultimately giving rise to fully mature effector

306   NK cells that are released into the bloodstream (**Fig. 6A**). Downstream of the pluripotent LKS

307   population, cells of the lymphoid lineage and the myeloid/erythroid lineage separate through the

308   common lymphoid progenitor (CLP; Lin^- $CD127^+$ $cKit^{lo}$ $Sca1^{lo}$) and the common myeloid

309   progenitor (CMP; Lin^- $CD127^-$ $cKit^+$ $Sca1^-$ $CD34^+$ $CD16/32^-$), respectively. Deriving from the

310   CLP, NK cells are generated first from the pre-NK progenitor (pre-NKP; Lin^- $CD127^+$ $CD27^+$

311     $CD122^-$ $CD244.2^+$), then the NKP (Lin^- $CD127^+$ $CD27^+$ $CD122^+$ $CD244.2^+$), which represents

312   what is thought to be the first fully committed cell of the NK lineage, and finally *bona fide* NK

313   cells that then begin to express NKp46, CD49b and CD11b (*54*). To investigate any potential

314   aberrations in NK cell development between WT and $CypD^{-/-}$ mice, we phenotyped the BM

315   precursors beginning at the LKS population and working towards more committed progenitors,

316   during homeostasis and upon infection. We observed no differences in the frequency or number

317   of LKS cells between groups (**Fig. 6B; Fig. S4F**), nor in the CLP (**Fig. 6C; Fig. S4G**).

318   Additionally, there were similar levels of the CMP and granulocyte-monocyte progenitor (GMP)

319   in WT and CypD-deficient mice (**Fig. S4H-I**). However, beginning at the NK cell-specific

320   progenitors, we observed a decrease in pre-NKP and NKP populations (**Fig. 6D-F**), as well as a

321   lower frequency of fully mature $CD11b^+$ $CD27^-$ expressing NK cells in the BM upon infection

14

322   (**Fig. 6G**; **Fig. S4J**). Thus, CypD mediates NK cell hematopoiesis and an inability to progress

323   through the NK cell lineage correlates with a lack of mature NK cells in the periphery.

324   *CypD$^{-/-}$* **NK cell progenitors express higher levels of p53 and undergo enhanced cell death in**

325   **the BM**

326   To investigate the potential mechanisms involved in the reduction of NK cell progenitors

327   in the BM of *CypD$^{-/-}$* mice, we evaluated both cellular proliferation and death (*55, 56*). Both at

328   steady-state and upon infection, CypD had no effect on proliferation of NK cell progenitors, as

329   determined by intracellular Ki67 expression (**Fig. S4K-L**). Interestingly, p53, a central regulator

330   of cell growth arrest and cell death in a variety of cell types (*57*), has recently been demonstrated

331   to interact with CypD in mitochondria to facilitate necrosis of structural cells (*58*), while also

332   antagonizing p53-dependent growth arrest in a tumour model, suggesting that CypD-deficiency

333   could increase p53 function (*59*). Moreover, enhanced expression or activity of p53 halts

334   lymphopoiesis, causes cell death specifically in the lymphoid lineage and leads to lymphopenia

335   (*60, 61*). We, thus, investigated the level of p53 in NK cell progenitors by flow cytometry and

336   found elevated p53 protein in *CypD$^{-/-}$* pre-NKPs (**Fig. 6H**) and NKPs (**Fig. 6I**), but not in effector

337   NK cells in the BM (**Fig. S4M**) or BAL (**Fig. S4N**). Using differential expression of

338   AnnexinV/NucSpot (a 7-AAD analogue), the upregulation of p53 correlated with an enhanced

339   percentage of death (AnnexinV$^+$ NucSpot$^+$) in NKP cells (**Fig. 6J**), but not in pre-NKP cells (**Fig.**

340   **S4O**). Collectively, our results suggest that CypD antagonizes p53 function and prevents p53-

341   mediated cell death to conserve NK cell lymphopoiesis and the generation of mature effector NK

342   cells.

343 **Mice deficient in CypD are more susceptible to IAV due to a lack of IL-22 production by**

344 **conventional NK cells**

345 Having established that CypD regulates NK cell hematopoiesis and that $CypD^{-/-}$ NK cells

346 are more phenotypically immature with altered transcriptomic and metabolic profiles, we finally

347 hypothesized that NK cells from these mice are functionally impaired and confer susceptibility to

348 IAV infection. As our RNA-seq data indicated impaired anti-inflammatory cytokine production

349 (e.g. IL-10) and wound healing/hemostasis pathways in CypD-deficient NK cells (**Fig. 4B-C**), we

350 speculated that altered cytokine production was responsible for the heightened susceptibility and

351 pulmonary tissue damage.

352 Upon IAV infection, NK cells are a well-known source of IFN-γ (*62, 63*). However, the

353 function of IFN-γ in response to IAV is controversial (*64-66*) and its potential role in disease

354 tolerance has not been studied. At day 7 post-IAV infection, we observed a significant decrease in

355 the levels of IFN-γ in the BAL of $CypD^{-/-}$ mice, which aligns with the increased pathology (**Fig.**

356 **7A**). Utilizing *ex vivo* stimulation of cells with PMA/ionomycin, we confirmed by intracellular

357 cytokine staining (ICS) that CD49b$^+$ NK cells from the BAL and spleen were substantial sources

358 of IFN-γ. At day 5 post-IAV infection, a significantly lower frequency of $CypD^{-/-}$ NK cells was

359 IFN-γ$^+$ (**Fig. 7B; Fig. S5A**). However, in line with a previous study (*66*), using $Ifngr^{-/-}$ mice, we

360 found no role for IFN-γ signaling in disease tolerance to IAV, with mice exhibiting similar amounts

361 of protein and number of erythrocytes in the BAL (**Fig. S5B-C**), although a significant increase in

362 total leukocytes was noted (**Fig. S5D**). To completely rule-out that the reduction in IFN-γ was

363 responsible for the damage in the CypD-deficient mice, we reconstituted the airways of WT and

364 $CypD^{-/-}$ mice with 100ng of IFN-γ intranasally (i.n.), or vehicle control, at 5 days p.i., collected the

365 BAL at 7 days p.i and characterized pulmonary damage. As expected, we observed a significant

16

366 increase in protein and erythrocytes in the BAL of CypD-deficient mice that received PBS

367 compared to WT mice, but there was no amelioration in either group that received IFN-γ (**Fig S5E-**

368 **F**). Collectively, these data confirm that, despite a reduction of NK cell-derived IFN-γ in CypD-

369 deficient airways post-IAV infection, IFN-γ was not responsible for the break in disease tolerance.

370 The production of IL-22 by NK cells plays a key role in protection of barrier sites through

371 the promotion of epithelial cell survival and proliferation, and is a correlate of immunity to IAV

372 (*29, 30*). Importantly, CD27$^-$ NK cells, which are reduced in the BAL of *CypD$^{-/-}$* mice, have been

373 shown to be the major source of IL-22 with NK cell subpopulations (*28*). Thus, we postulated that

374 a lack of IL-22 production by CypD-deficient NK cells was underlying their susceptibility to IAV

375 infection. To assess this hypothesis, we began by confirming a previous study (*30*), showing that

376 IL-22-deficient mice had enhanced lung damage, indicated by elevated protein and cell

377 accumulation in the BAL, as well as pulmonary inflammation by histology at 7 days post-IAV

378 infection (**Fig. S5G-I**). Next, we measured the level of IL-22 in the BAL of WT and *CypD$^{-/-}$* mice

379 at various time points p.i. and found a significant reduction of IL-22 in *CypD$^{-/-}$* mice at 7 days p.i.

380 (**Fig. 7C**). Moreover, as with IFN-γ, we identified NK cells as an important source of IL-22 and

381 there was a specific reduction of IL-22$^+$ NK cells in both the BAL and spleen of CypD-deficient

382 mice compared to WT (**Fig. 7D; Fig. S5J**). These data collectively confirm the importance of

383 CypD within CD49b$^+$ conventional NK cells in IL-22 production.

384 Because of the observation that IL-22 is involved in disease tolerance to IAV and that

385 *CypD$^{-/-}$* mice have reduced IL-22 in the airways, we investigated whether or not reconstitution of

386 CypD-deficient mice with IL-22 could protect against IAV infection by limiting lung tissue

387 damage. At 5 days post-lethal IAV infection, we intranasally reconstituted the airways of WT and

388 *CypD$^{-/-}$* mice with 100ng of IL-22 or PBS (**Fig. 7E**) and assessed mortality. As expected, *CypD$^{-/-}$*

389 mice that received PBS were significantly more susceptible than WT mice that received PBS.

390 Strikingly, after IAV infection, the survival of CypD-deficient mice that received exogenous IL-

391 22 was significantly increased and comparable to both WT groups (**Fig. 7F**). This enhanced

392 survival was independent of host resistance (**Fig. 7G**), but dependent on disease tolerance as the

393 increased levels of erythrocyte influx and fibrosis were abrogated in the CypD-deficient mice (**Fig.**

394 **7H-I**; **Fig. S5K**). Finally, having established the role of IL-22 in enhancing disease tolerance in

395 *CypD$^{-/-}$* mice, as well as an inability of CypD-deficient NK cells to produce IL-22, we sought to

396 directly assess the capacity of WT versus *CypD$^{-/-}$* NK cells to protect against tissue damage in an

397 IL-22-deficient environment. To do this, we purified NK cells from naïve spleens of WT and

398 CypD-deficient hosts, then transferred them (1×10^5 cells) intratracheally into infected *Il22$^{-/-}$* hosts

399 at 5 days post-IAV infection, as to not affect early viral replication or the onset of tissue damage.

400 At 7 days p.i. (2 days post-transfer), we collected the BAL and lungs, then assayed damage and

401 viral loads (**Fig. 7J**). We found that IL-22-deficient mice that received WT NK cells exhibited

402 statistically significantly enhanced disease tolerance, as assessed by attenuated protein and

403 erythrocyte accumulation in the BAL, while no improvement was noted in mice receiving *CypD^{-}*

404 *$^{/-}$* NK cells compared to PBS controls (**Fig. 7K-L**). In line with IL-22 acting primarily on structural

405 cells, no variance in total leukocyte counts was observed in any group (**Fig. 7M**). Furthermore, no

406 differences in viral load between any group could be delineated; thus, disease tolerance, rather

407 than host resistance, was responsible for the reduced airway damage (**Fig. 7N**). Collectively, these

408 data indicate that NK cell-derived IL-22 is dependent upon *CypD* expression and is required for

409 regulating disease tolerance following IAV infection.

410

DISCUSSION

The immune response to influenza requires a tightly regulated effort from both the innate and adaptive branches. Shortly following infection, early innate cells infiltrate the airways, and along with resident immune cells, coordinate to inhibit IAV replication and elimination (host resistance) from the lung. These host resistance mechanisms to IAV are well studied (*67*) and current influenza therapies, such as oseltamivir, exclusively target viral replication/dissemination to assist these pathways (*68*). However, host resistance comes at a substantial immunopathological cost that often is the cause of disease severity and mortality; therefore, limiting tissue damage and maintaining the functional capacity of the lung (disease tolerance) is critical for host survival. Breaks in disease tolerance cause mortality through loss of the integrity of the pulmonary epithelial/endothelial barrier, hemorrhaging and airway remodelling, all of which ultimately compromise gas exchange and lung physiology. Thus, the regulatory mechanisms of host defense against infection require a tight balance of generating immunity to resist a pathogen, while not compromising the physiology of infected organs that must be returned to homeostasis.

Disease tolerance as a defense strategy was initially established in plants (*69*) and has since been extended to mammals (*1, 3*). Evidence for its importance during chronic disease such as *Mycobacterium tuberculosis* and helminthic infections (*70, 71*) is accumulating, along with an understanding of the underlying mechanisms. Yet, our knowledge of disease tolerance pathways against acute viral infections like IAV remains limited. We and others have recently provided some insight into the importance of maintaining tissue integrity in disease tolerance to IAV either through the production of the host lipid mediator LTB_4 (*16*) or inhibition of pulmonary matrix metalloproteases (*17*). In the current study, we extend the fundamental observation that reducing tissue damage is essential in disease tolerance and we define an role for CypD in this process,

434   namely, by regulating NK cell generation in the bone marrow as well as promoting their effector

435   functions in the airways. This work adds further evidence to our earlier studies that highlighted

436   CypD as an essential component of lymphocyte-mediated host defense during infection (*72, 73*),

437   in addition to its well-documented roles in necrosis (*74*) and the progression of neurological

438   disorders, including multiple sclerosis (*75*).

439   The unique location of CypD within the mitochondrial matrix places it at the intersection

440   of several essential cellular processes during health and disease. For example, in mature

441   leukocytes, the mitochondrial antiviral signaling protein (MAVS) is anchored to the outer

442   mitochondrial membrane and is essential for the induction of IFN-I in response to several viruses,

443   including IAV. Although activation of the cytosolic pattern recognition receptor (PRR) RIG-I by

444   viral RNA is the major trigger of MAVS-mediated responses, mitochondrial heat shock proteins,

445   fission proteins and mitochondria-derived ROS critically regulate MAVS function (*76*).

446   Additionally, IAV-encoded PB1-F2 localizes to the mitochondria and induces early intrinsic

447   apoptosis to temper antiviral responses that is neutralized by the host NOD-like receptor NLRX1

448   (Nucleotide-binding, leucine-rich repeat containing X1) within the mitochondrial matrix (*35*).

449   During LCMV infection, enhanced mitochondrial oxidative phosphorylation promotes antiviral

450   immunity by pDCs (*77*), while our recent study highlighted the importance of CypD-dependent

451   metabolic changes in T cell responses to promote disease tolerance to *Mtb* (*72*). Thus,

452   mitochondria are critical orchestrators of both resistance and tolerance mechanisms in ways that

453   are cell- and pathogen-specific.

454   Although the majority of previous work has focused on mitochondria in mature leukocytes,

455   this study also revealed a role for mitochondrial CypD in regulating lymphopoiesis and p53-

456   associated progenitor cell death. In structural cells, p53, an essential regulator of cell survival and

457 death, was previously shown to translocate to the mitochondrial matrix and interact with CypD,

458 resulting in necrotic cell death (*58*). Interestingly, enhancement of p53 activity specifically within

459 lymphocyte progenitors has been shown to induce cell death and skew hematopoiesis towards

460 myelopoiesis (*60, 61*). Our results uncovered a hitherto unappreciated inhibition of p53 by CypD

461 in NK cell progenitors to promote lymphopoiesis, akin to the role previously described for Mysm1

462 and Mdm2 (*60, 61*). Importantly, we and others have described hematopoietic progenitor cell death

463 as an emerging master regulator of bias between lymphopoiesis and myelopoiesis (*55, 78, 79*).

464 Though no direct protein-protein interaction experiments between p53 and CypD were attempted

465 in our study, it is intriguing to speculate that a balance between lymphopoiesis and myelopoiesis

466 signals in progenitors may alter the outcome of p53/CypD interactions in the mitochondria, either

467 by promoting or antagonizing p53-dependent lymphoid progenitor cell death as the leukocyte

468 requirements change in the periphery. Certainly, more studies are required to fully delineate the

469 contributions of CypD and p53 to hematopoiesis, as well as other known regulators such as Mysm1

470 and Mdm2.

471 In addition to our results in the bone marrow, we equally identified a function for CypD in

472 mature NK cells that promotes their activation and function. NK cells are well known for their

473 tumoricidal capacity and cytotoxicity against virally-infected cells, through an "innate" non-MHC

474 restricted manner, which differs from cytolytic CD8 T cells (*19*). The importance of NK cells in

475 the immune response to IAV is well-documented and appears to participate in both host resistance

476 and disease tolerance. For example, complete genetic ablation of NK cells (via knockout of the

477 transcription factor Nfil3; *Nfil3$^{-/-}$* mice) (*22*), loss of the HA interacting receptor NKp46 (*Nkp46$^{-/-}$*

478) (*23*), or depletion using an anti-asialo GM1 antibody (*24*) all result in IAV-induced lethality and

479 elevated viral titres in the lung. Thus, NK cells are required for host resistance to IAV through

21

480   HA/NKp46 cell lysis. While it has been recently shown that IL-22 production by NK cells limits

481   pulmonary immunopathology during IAV infection (*29*), the regulatory mechanisms were

482   unknown. Here, we found that CypD regulates IL-22 production by NK cells in the lung (**Fig. 7C-**

483   **D**; **Fig. S5K**), while expression of perforin and granzyme B by NK cells (**Fig. 2H**) and viral load

484   (**Fig. 1C**) were unaffected. Therefore, during the course of IAV infection, the functional capacity

485   of NK cells is dynamic and can be changed from promoting resistance to tolerance.

486   Early NK cell responses, beginning at approximately 2 days post-IAV infection, appear to

487   be mediated by NKp46 and are primarily concerned with restricting viral replication by killing

488   infected cells, which correlates with the onset of symptoms. Thus, studies using mice that lack NK

489   cells or NKp46 expression prior to the onset of infection show enhanced mortality coupled with

490   increased viral loads (*22-24*). Following viral containment, NK cells may shift to a disease

491   tolerance role that is marked by production of IL-22 beginning at around day 5 post-infection. Our

492   results suggest that during the early phase of infection, the function of NK cells in host resistance

493   is CypD-independent, while at the later stage of infection the function of NK cells in disease

494   tolerance is mediated by CypD. As our RNA-Seq and functional data (**Fig. 3G**; **Fig. 3I-P**)

495   highlighted elevated reliance on OXPHOS in $CypD^{-/-}$ NK cells compared to WT, we propose that

496   a CypD-dependent metabolic shift in NK cells may, in part, dictate the transition of their effector

497   program from host resistance to disease tolerance. Additional investigation is required to identify

498   the intrinsic and/or extrinsic cues leading to the alteration in NK cell function during infection.

499   Greater consideration of the kinetics of infection may also serve to explain discrepancies

500   in the source of IL-22 during IAV infection. IL-22 can be produced by several lymphocyte

501   populations in response to IAV, including NK cells, NKT cells, ILCs and conventional αβ T-cells.

502   Studies investigating the early phase of infection (i.e. 2 and 4 days p.i.) elucidated NKT and ILCs

22

503   as the major sources (*26, 27*), while our and other's work at the late phase of infection (i.e. day 5

504   and day 7) (*29*) showed conventional NK cells as the major source of IL-22. Collectively, these

505   results suggest that early IL-22 production is dominated by NKT cells and ILCs, while NK cells

506   are contributing to host resistance. However, at later stages of infection there is a shift in the

507   function of NK cells highlighted by a production of IL-22, which contributes to disease tolerance.

508   Although speculative, this concept is supported by our adoptive transfer experiments of NK cells

509   into IL-22-deficient mice, where we show that CypD-dependent production of IL-22 by NK cells

510   is sufficient to promote disease tolerance against IAV infection. Whether or not CypD solely

511   regulates IL-22 production in NK cells rather than other cell types, or if its role is IAV-specific

512   remains unknown. Undoubtedly, further insight into the kinetics of the source of IL-22 during IAV

513   infection and how leukocyte function changes over time are required to more completely

514   understand this complex phenomenon.

515   Our results outline an important role for CypD in NK cell development in the bone marrow

516   as well as NK cell function in the airways. Although our work indicates separate roles for CypD

517   in bone marrow NK cell progenitors and in mature NK cells, the exact mechanisms by which CypD

518   functions and whether these two phenotypes are connected or separate require further

519   investigation. The usage of a conditional knockout, rather than a constitutive knockout used in this

520   study, that specifically deletes CypD in either mature NK cells or in bone marrow progenitors,

521   could help to address these questions. Alternatively, mounting evidence suggests that progenitors

522   may be imprinted in the bone marrow and this signature may affect the function of terminally

523   differentiated effector cells in a process termed "trained immunity" (*80*). Thus, NK cells in the

524   periphery of $CypD^{-/-}$ mice may be imprinted with an immature phenotype because of the lack of

525   CypD function in bone marrow NK cell progenitors. We have recently described systemic BCG

526 vaccination reprograms hematopoietic stem cells to promote myelopoiesis and generate more

527 protective macrophage responses to subsequent *Mtb* infection (*79, 81*). Interestingly, NK cells

528 have equally been shown to be "trained" by BCG (*82*), and memory NK cells are generated

529 following IAV infection (*22*). Thus, it is possible that CypD may play a role in protective NK cell

530 imprinting in the bone marrow. The potential of trained immunity during IAV infection is an

531 exciting field for further research.

532 Influenza infections are persistent human pathogens, being responsible yearly for

533 approximately 1 billion infections and between 300 000-500 000 deaths worldwide (*68*). Past IAV

534 pandemics, as well as the current COVID-19 pandemic, have highlighted the importance of

535 understanding host-pathogen interactions during acute respiratory infections. As we continue to

536 better appreciate the interplay between host resistance (early responses) and disease tolerance (late

537 responses), targeted therapies require an appropriate timeline for administration. For instance, our

538 recent studies investigating host immunotherapy via the eicosanoid/IFN-I axis showed early

539 inhibition of mPGES-1 (the enzyme involved in prostaglandin E_2 production) increased antiviral

540 IFN-β production to enhance host resistance (*83*). On the other hand, late-stage administration of

541 exogenous LTB_4 potentiates immunomodulation of IFN-α signaling to promote disease tolerance,

542 without affecting antiviral responses (*16*). Considering that higher levels of lung

543 immunopathology, rather than viral replication, is the major cause of morbidity and mortality

544 during severe SARS-CoV-2 and IAV infections (*10, 84*), therapies that target disease tolerance

545 may provide a more universal benefit compared to specific antiviral therapies. Studies that outline

546 novel pathways of disease tolerance are required and will contribute to the next generation of

547 respiratory virus therapies.

548

MATERIALS AND METHODS

Mice

Six- to ten-week-old C57BL/6, CD45.1 and *Ifngr*$^{-/-}$ mice were purchased from Jackson Laboratories. *CypD*$^{-/-}$ mice were provided by M. Forte (Oregon Health and Science University, Portland, OR, USA). All animals were housed and inbred at the animal facility of the Research Institute of McGill University. Experiments were performed using age- and sex-matched mice.

Viruses & Infection

All *in vivo* infections were performed using mouse adapted influenza A/Puerto Rico/8/34 (H1N1) virus (IAV), kindly provided by Dr. Jonathan A. McCullers (St. Jude Children Research Hospital). Mice were challenged intranasally (in 25μL PBS) with IAV at a sublethal dose of 50 PFU or a lethal dose (LD$_{50}$) of 90 PFU. 90 PFU was used for the survival experiments in **Fig. 1A** and **Fig. 7F**. For all other experiments, 50 PFU was used. During survival experiments mice were monitored twice daily for signs of duress and weighed daily. Mice reaching 75% of original body weight were considered moribund and sacrificed. Viruses were propagated and isolated from Madin-Darby Canine Kidney (MDCK) cells and titrated using standard MDCK plaque assays. MDCK cells were obtained from the American Type Culture Collection and maintained in Dulbecco's modified Eagle medium enriched with 10% (*v/v*) FBS, 2 mM L-glutamine and 100 U ml^{-1} penicillin/streptomycin.

25

Protein in the BAL

BAL were collected by cannulating the trachea with a 22-gauge cannula, then washing the lungs with 3×1 ml of cold, sterile PBS. The total volume recovered after lavage was ~0.7 ml. Samples were spun down (1,500 r.p.m.; 10 min) and the total protein content was assessed by Pierce BCA Protein assay (Thermo Fisher Scientific).

Texas Red-Dextran Lung Permeability

WT and $CypD^{-/-}$ were infected for 7 days with 50 PFU. On day 7, mice were delivered 25µL of 50mg/mL (1.25mg) Texas Red-Dextran (10 000 MW) intranasally. 1 hour later mice were sacrificed and lungs were carefully excised without damaging. Lungs were imaged using the In Vivo Xtreme (Bruker) using fluorescence capture. Resulting images were then analyzed for total fluorescent intensity of lung images using ImageJ software (National Institutes of Health). During the 1 hour of incubation Texas Red-Dextran molecules diffused into the blood of infected mice, due to the loss of epithelial/endothelial barrier integrity. Therefore, lower fluorescence is indicative of increased damage and compromised barrier integrity.

Generation of chimeric mice

CD45.1$^+$ B6 mice or $CypD^{-/-}$ mice were lethally irradiated with 9 Gy following 3 days of antibiotic treatment (0.5g Enrofloxacin (Bayer) per litre of drinking water). 16 hours later, the BM compartment was reconstituted with 4×10^6 nucleated cells from either CD45.1$^+$ mice ($CypD^{-/-}$ recipient) or $CypD^{-/-}$ mice (CD45.1$^+$ recipient) and antibiotic treatment was maintained for 2 additional weeks. Between 10-12 weeks post-injection, reconstitution was validated by flow cytometry and was >90%. Mice were then infected for downstream assays.

Flow Cytometry

590

591 Lung tissues were perfused with 10 mL of PBS, harvested and minced before collagenase digestion

592 (150 U mL^{-1}) for 1 h at 37 °C. Lungs were passed on a 40 µm nylon mesh, and red blood cells

593 were lysed. For bone marrow staining, cells were isolated following aseptic flushing of the tibiae

594 and femurs, and red blood cells were lysed. BAL were collected as previously described, spun

595 down and red blood cells lysed. Spleens were aseptically removed, crushed on a 40 µm nylon

596 mesh, and red blood cells were lysed. Then total cell counts were determined with a

597 hemocytometer. In some experiments BAL were counted prior to red blood cell lysis to enumerate

598 erythrocyte influx into the airways and then red blood cells were lysed. For peripheral blood

599 staining, the blood was collected by cardiac puncture in a BD Microtainer tube and stained

600 extracellularly; red blood cells were then lysed.

601 Cells were initially stained with eFluor-506 viability dye in PBS (eBioscience; 20 min; 4 °C),

602 washed and surface stained with anti-CD16/32 (BD Biosciences) in 0.5% BSA/PBS solution to

603 block non-specific antibody interactions with Fc receptors (10 min; 4 °C). Cells were then surface

604 stained with combinations of PE-CF594-conjugated anti-SiglecF, BUV395-conjugated anti-

605 CD11b, PerCP-eFluor780- or AlexaFluor700-conjugated anti-Ly6G, fluorescein isothiocyanate

606 (FITC)- or allophycocyanin (APC)-conjugated anti-Ly6C, APC-eFluor780-conjugated anti-F4/80,

607 BV421-conjugated anti-CD11c, FITC- or BUV395-conjugated anti-CD45.2 or APC-conjugated

608 anti-CD45.1, Pe-Cy7-conjugated anti-CD3, BV786-conjugated anti-CD127, APC- or BUV737-

609 conjugated anti-NKp46, BV421-conjugated anti-CD49b, PE-conjugated anti-CD49a (all from BD

610 BioScience, except anti-Ly6G from eBioscience), or PE-Cy7-conjugated (BD Biosciences) or

611 FITC-conjugated (eBioscience) anti-CD27. Cells were then fixed with 1% PFA for 1 hour, washed

612 and acquired in 0.5% BSA/PBS solution.

27

613   In some experiments, following extracellular staining, samples were stained intracellularly for

614   Ki67, active Caspase 3, perforin, granzyme B or p53. For APC-conjugated anti-Ki67, or anti-

615   perforin and PE-conjugated anti-active Caspase 3, or anti-granzyme B (all from BD Biosciences)

616   cells were initially fixed and permeabilized using BD Cytofix/Cytoperm (BD Biosciences) for 30

617   minutes at 4° C and then stained for 1 hour. Cells were washed and acquired. For p53 staining,

618   cells were initially fixed and permeabilized for 1 hour using the Foxp3/Transcription Factor

619   Staining Buffer Set (eBioscience) and then stained using the PE-conjugated anti-p53 Set (BD

620   Biosciences), according to the manufacturer's instructions. The provided PE-conjugated isotype

621   was used as a control.

622   In experiments involving bone marrow progenitors, cells were processed, counted, stained for

623   viability and blocked as before. Cells were then stained with biotin conjugated anti-Ly6C/G, anti-

624   CD5, anti-B220, anti-Ter119, anti-CD4 and anti-CD8 for 20 minutes at 4° C. Cells were then

625   washed and stained with APC-Cy7-conjugated streptavidin, APC-conjugated anti-cKit, PE-Cy7-

626   conjugated Sca-1 for LKS cells. For CMP/GMP experiments, cells were not blocked and instead

627   FITC-conjugated anti-CD34 and PerCP-eFluor780-conjugated anti-CD16/32 (all from BD

628   Biosciences, except anti-CD16/32 from eBioscience) were added to the previous cocktail. For NK

629   cell progenitors, PE-CF594-conjugated anti-CD122 and BUV395-conjugated anti-CD244.2 were

630   added along with anti-CD27 and anti-CD127 (BD Biosciences) as previously described.

631   Finally, for experiments involving intracellular cytokine staining (ICS), 2×10^6 single splenocytes

632   or BAL cells were incubated for 4 hours at 37° C in the presence of PMA/Ionomycin and Brefeldin

633   A (Cell Activation Cocktail; BioLegend) or GolgiPlug control (BD Biosciences). Cells were then

634   stained extracellularly, fixed and permeabilized using BD Cytofix/Cytoperm (BD Biosciences),

635 before being stained intracellularly for PE-conjugated anti-IL-22 and APC-conjugated anti-IFN-γ

636 (BD Biosciences).

637 Flow cytometry acquisition was performed using BD LSRFortessa X-20 (BD Biosciences) with

638 FACSDiva Software version 8.0.1 (BD Biosciences). Analysis was performed using FlowJo

639 software version 10 (Tree Star).

640 **Evaluation of mitochondrial fitness using Mitotracker Green/Orange and Mitosox Red**

641 Single cell suspensions were stained with extracellular antibodies as described above and then with

642 Mitotracker Green and Orange 150nM, or MitoSox Red 1μM (Invitrogen technologies) in PBS for

643 30 min at room temperature and then washed with PBS. For experiments involving mitochondrial

644 potential, dysregulated mitochondria were Mitotracker Green^{hi} and Mitotracker Orange^{lo}, while

645 respiring mitochondria were considered as Mitotracker Green^{hi} and Mitotracker Orange^{hi} as

646 previously described (*85*)

647 **Extracellular Flux Analysis**

648 Real-time oxygen consumption rates (OCR) of purified splenic NK cells were measured in XF

649 media (non-buffered DMEM containing 2mM L-glutamine, 25mM glucose and 1mM sodium

650 pyruvate) using a Seahorse XFe 96 Analyzer (Agilent Technologies). For the mitochondrial stress

651 test, mitochondrial inhibitors oligomycin, fluorocarbonyl cyanide phenylhydrazone (FCCP),

652 antimycin A and rotenone were used, as per the manufacturer's recommendations. Briefly, NK

653 cells were seeded at a density of 200 000 cells per well and 3 basal measurements were taken.

654 Following this, 2 consecutive measurements were taken following each injection of oligomycin,

655 FCCP, and antimycin A with rotenone. All measurements were normalized to cell number using a

29

656   crystal violet dye extraction assay. Oxygen consumption curves were generated using Wave

657   Desktop 2.3 (Agilent Technologies). Basal OCR was calculated by subtracting measurement 7

658   (non-mitochondrial respiration) from measurement 1. Maximal respiration was calculated by

659   subtracting measurement 7 (non-mitochondrial respiration) from measurement 5 and spare

660   respiratory capacity was the difference between maximal respiration and basal rate.

661   **Adoptive transfer model**

662   NK cells were purified from uninfected spleens of WT and $CypD^{-/-}$ mice using the EasySep Mouse

663   NK Cell Isolation Kit (Stem Cell Technologies) according to the supplier's recommendations.

664   Sorted cells were counted, washed (cold sterile PBS) and normalized to $1x10^5$ cells/50µL of sterile

665   PBS. Purity was verified by flow cytometry and purity was always over 85% NK cells prior to

666   transfer. NK cells were then transferred into $Il22^{-/-}$ mice on day 5 post-infection (50 PFU) via the

667   intratracheal route. 2 days later, BAL were harvested for lung damage assays and, lungs were

668   harvested for viral load analysis or histology.

669   **IL-22 or IFN-γ treatment**

670   Recombinant murine IL-22 or IFN-γ was purchased from Peprotech. Mice were intranasally

671   infected with 50 PFU of IAV. On day 5 post-infection, mice were given either PBS, IL-22 or IFN-

672   γ (both 100ng/25µL) intranasally. Mice were sacrificed on day 7 post-infection, and the lungs were

673   harvested and processed to determine the pulmonary viral load, or the BAL collected for damage

674   assays. In some experiments, mice were infected with 90 PFU and IL-22 was delivered as stated

675   and survival was monitored.

676

Histopathological analysis

Lungs were inflated with and fixed for 48 h in 10% formalin, then embedded in paraffin. Next, 5 µm sections were cut and stained with Haematoxylin and Eosin or Masson's Trichrome. Slides were scanned at a resolution of 20× magnification and pictures were taken using a Leica Aperio slide scanner (Leica). Quantification of collagen-afflicted areas on Masson's Trichrome stained slides was performed using ImageJ software (National Institutes of Health) as previously described (*86*).

Total bioactive IFN-I assay

Secretion of total active IFN-I (both IFN-α and IFN-β) in cell culture supernatants was assessed using the B16-Blue IFN-α/-β reporter cell line for murine samples (from InvivoGen), according to the specifications of the manufacturer. B16 cells were maintained in RPMI supplemented with 10% (*v/v*) FBS, 2 mM L-glutamine and 100 U ml^{-1} penicillin/streptomycin.

Cell death analysis

Lactate dehydrogenase release in the BAL of IAV-infected mice was quantified using the CytoTox 96 Non-Radioactive Cytotoxicity Assay (Promega), per the manufacturer's recommendations. Dead cell levels *in vivo* were assessed using PE-AnnexinV (BioLegend) and NucSpot Far-Red (Biotium), according to the manufacturer's instructions and unfixed cells were acquired immediately by flow cytometry.

31

697   **Wet-to-dry ratio**

698   Lungs were harvested from naïve or IAV-infected mice (50 PFU; day 7 post-infection), and blood

699   clots were carefully removed. Then, the lungs were weighed (wet weight) and dried in an oven

700   (56 °C, 2 d; dry weight), and the dry weight was measured. Data are presented as the ratio of wet

701   weight to dry weight.

702   **RNA isolation and reverse transcription quantitative PCR (qPCR)**

703   RNA from purified NK cells was extracted using RNeasy Kit (Qiagen) according to the

704   manufacturer's instructions. Some 500 ng of RNA were reverse transcribed using the ABM 5X

705   RT MasterMix (Applied Biological Materials), as directed by the manufacturer. Complementary

706   DNA was generated by qPCR using BrightGreen SYBR Green (Applied Biological Materials). Cq

707   values obtained on a CFX96 PCR System (Bio-Rad) were analysed using $2^{-\Delta Cq}$ formula

708   normalizing target gene expression to *Gapdh*.

709   **Library preparation and RNA-sequencing**

710   Bulk RNA was collected from purified, splenic NK cells from 5 WT (1 control, 4 IAV-infected)

711   and 5 *CypD$^{-/-}$* mice (1 control, 4 IAV-infected). Sequencing libraries were constructed using the

712   the Illumina TruSeq protocol. Libraries were sequenced on an Illumina NovaSeq (paired-end 100

713   base pair) to an average depth of 42.6 million reads per sample. Adapter sequences and low-quality

714   score bases were trimmed from reads using Trim Galore (v0.6.2, Cutadapt v2.2) (*87*) in paired-

715   end mode (-q 20 --paired --phred33). Trimmed reads were pseudoaligned to the *Mus musculus*

716   reference transcriptome (mm10.81, downloaded from Ensembl) using the quant function in kallisto

717   (v0.43) (*88*) in paired-end mode (average of 24.7 million pseudoaligned reads per sample). Gene-

718   level expression estimates accounting for the average transcript length across samples were

719   calculated using the R (v3.6.3) package tximport (v1.14.2) (*89*).

Modeling the effect of the *CypD$^{-/-}$* genotype on gene expression

721   Expression data was filtered for protein-coding genes that were sufficiently expressed across all

722   samples (median logCPM > 1), leaving 12,451 genes for downstream analysis. After removing

723   non-coding and lowly-expressed genes, normalization factors to scale the raw library sizes were

724   calculated using calcNormFactors in edgeR (v3.26.8) (*90*). The voomWithQualityWeights

725   function in limma (v3.40.6) (*91*) was used to apply these size factors, estimate the mean-variance

726   relationship, convert counts to logCPM values, and estimate sample-specific observational weights

727   that take into account variation in sample quality.

728   The following nested linear model was used to identify genes for which expression levels

729   are differentially-expressed between WT and *CypD$^{-/-}$* mice within each condition:

730    $$M_1: E(i,j) \sim \begin{cases} \beta_0(i) + \beta_{CypD}^{ctl}(i) \cdot CypD(j) + \beta_{M\_aligned}(i) \cdot M\_aligned(j) + \varepsilon^{ctl}(i,j) \text{ if Condition} = ctl \\ \beta_0(i) + \beta_{flu}(i) + \beta_{CypD}^{flu}(i) \cdot CypD(j) + \beta_{M\_aligned}(i) \cdot M\_aligned(j) + \varepsilon^{flu}(i,j) \text{ if Condition} = flu \end{cases}$$

731   Here, *E(i,j)* represents the expression estimate of gene *i* for individual *j*, $\beta_0(i)$ is the global

732   intercept accounting for the expected expression of gene *i* in a control WT mouse, $\beta_{CypD}^{ctl}(i)$ and

733    $\beta_{CypD}^{flu}(i)$ indicate the effects of the *CypD$^{-/-}$* genotype on gene *i* within each condition, and $\beta_{flu}(i)$

734   represents the intrinsic infection effect of IAV infection. Further, *M_aligned* represents the mean-

735   centered, scaled (mean = 0, standard deviation = 1) number of pseudoaligned reads per sample (in

736   millions), with $\beta_{M\_aligned}$ being the impact of read depth on expression. Finally, ε^{cdt} represents the

737   residuals for each respective condition (*ctl* or *flu*) for each gene *i*, individual *j* pair. The model was

738   fit using the lmFit and eBayes functions in limma, and the estimates of the genotype effect ($\beta_{CypD}^{ctl}(i)$

33

739 and $\beta_{CypD}^{flu}(i)$) were extracted across all genes, along with their corresponding p-values. These

740 estimates represent the genotype-related (WT vs $CypD^{-/-}$) differential expression effects within

741 each condition. We controlled for false discovery rate (FDR) using an approach analogous to that

742 of Storey and Tibshirani (*92, 93*), which derives the null distribution empirically. To obtain a null,

743 we performed 10 permutations, where genotype label (WT or $CypD^{-/-}$) was permuted within

744 infection condition (control or IAV-infected). We considered genes significantly differentially-

745 expressed between genotypes if they had a β_{CypD}^{ctl} or β_{CypD}^{flu} |logFC| > 0.5 and an FDR < 0.10. Of

746 note, all of our downstream analyses focused only on the $CypD^{-/-}$ effect in the IAV-infected

747 condition (β_{CypD}^{flu}).

Gene set enrichment analyses

749 Gene set enrichment analysis was performed using two independent methods, fgsea (*94*) and

750 ClueGO (*95*), depending on the type of data being evaluated. The enrichment program

751 specifications and the data in which they were used to assess enrichments are described below:

752 The R package fgsea (v1.10.1) was used to perform gene set enrichment analysis for the genotype

753 effects using the H hallmark gene sets (*96*). Input t-statistics were obtained directly from the

754 topTable function in limma. These t-statistics were then ranked and used to perform the enrichment

755 tests with the following parameters: minSize = 15, maxSize = 500, nperm = 100000. Enrichments

756 scores (ES) and Benjamini-Hochberg adjusted p-values output by fgsea were collected for each

757 tested gene set.

758 Gene set enrichment analysis was also performed for our lists of differentially-expressed (DE)

759 genes between the WT and $CypD^{-/-}$ mice in the influenza-infected condition using the ClueGO

760　(v2.5.7) (Bindea et al., 2009) Cytoscape (v3.7.1) (*97*) module in functional analysis mode, where

761　the target set of genes was either the list of genes showing higher expression in the WT or *CypD⁻*

762　*⁄⁻* mice and the background set was the list of all genes tested. Specifically, we tested for the

763　enrichment of GO terms related to biological processes (ontology source: GO_BiologicalProcess-

764　EBI-UniProt-GOA-ACAP-ARAP_08.05.2020_00h00) using the following parameters: visual

765　style = Groups, default Network Specificity, no GO Term Fusion, min. GO Tree Interval level =

766　3, max. GO Tree Interval level = 8, min. number of genes = 2, min. percentage of genes = 4.0,

767　statistical test used = Enrichment (right-sided hypergeometric test), p-value correction =

768　Benjamini-Hochberg. For the graphical representation of the enrichment analysis, ClueGO

769　clustering functionality was used (kappa threshold score for considering or rejecting term-to-term

770　links set to 0.4). Only pathways with an FDR < 0.01 are reported.

771　To test for an enrichment of WT or *CypD⁻⁄⁻* DE genes in the IAV-infected condition among genes

772　known to be involved in tissue repair and wound healing (TiRe gene set, curated from Yanai et al.

773　(Yanai et al., 2016), n = 220 retained in our dataset), we calculated the proportion in our WT or

774　*CypD⁻⁄⁻* DE gene lists that also fall into the TiRe gene set and considered this our "observed

775　proportion". To obtain a null distribution, we performed 1,000 permutations where, for each

776　iteration, we: i) sampled the same number of genes as DE genes in our set (146 for WT and 169

777　for *CypD⁻⁄⁻*) from a list of all genes tested, and ii) calculated the proportion of these genes that are

778　also in the TiRe gene set (our "null percentage"). P-values were computed by evaluating the

779　number of permutations in which the null percentage was greater than or equal to the observed

780　percentage divided by the number of total permutations (n = 1,000).

781

782 **ELISA**

783 IFN-β levels in infected lungs and BAL were measured using a VeriKine Mouse IFN-β ELISA kit

784 (PBL Assay Science). IFN-γ and IL-22 levels were assessed by ELISA (R&D Systems), as

785 directed by the manufacturer.

786 **Statistical analysis**

787 Data are presented as means ± s.e.m. Statistical analyses were performed using GraphPad Prism

788 version 8.0.2 software (GraphPad). Statistical differences were determined using a two-sided log-

789 rank test (survival studies), one-way analysis of variance (ANOVA) followed by Sidak's multiple

790 comparisons test, two-way ANOVA followed by Dunnett's or Tukey's multiple comparisons test,

791 or two-tailed Student's T-Test, as outlined in the Figure Legends. Significance is denoted by *

792 p<0.05, ** p<0.01, ***p<0.001, ****p<0.0001.

793 **Ethics**

794 All experiments involving animals were approved by McGill University (permit number 2010-

795 5860) in strict accordance with the guidelines set out by the Canadian Council on Animal Care.

796

797

798

799

800

801

802

803

804

36

REFERENCES

1. R. Medzhitov, D. S. Schneider, M. P. Soares, Disease tolerance as a defense strategy. *Science* **335**, 936-941 (2012).
2. R. Martins *et al.*, Disease Tolerance as an Inherent Component of Immunity. *Annu Rev Immunol* **37**, 405-437 (2019).
3. D. S. Schneider, J. S. Ayres, Two ways to survive infection: what resistance and tolerance can teach us about treating infectious diseases. *Nature Reviews Immunology* **8**, 889-895 (2008).
4. I. Meunier, E. Kaufmann, J. Downey, M. Divangahi, Unravelling the networks dictating host resistance versus tolerance during pulmonary infections. *Cell Tissue Res* **367**, 525-536 (2017).
5. E. Bautista *et al.*, Clinical aspects of pandemic 2009 influenza A (H1N1) virus infection. *N Engl J Med* **362**, 1708-1719 (2010).
6. L. A. Perrone, J. K. Plowden, A. Garcia-Sastre, J. M. Katz, T. M. Tumpey, H5N1 and 1918 pandemic influenza virus infection results in early and excessive infiltration of macrophages and neutrophils in the lungs of mice. *PLoS Pathog* **4**, e1000115 (2008).
7. M. Brandes, F. Klauschen, S. Kuchen, R. N. Germain, A systems analysis identifies a feedforward inflammatory circuit leading to lethal influenza infection. *Cell* **154**, 197-212 (2013).
8. N. H. Leung, C. Xu, D. K. Ip, B. J. Cowling, Review Article: The Fraction of Influenza Virus Infections That Are Asymptomatic: A Systematic Review and Meta-analysis. *Epidemiology* **26**, 862-872 (2015).
9. L. Zou *et al.*, SARS-CoV-2 Viral Load in Upper Respiratory Specimens of Infected Patients. *N Engl J Med* **382**, 1177-1179 (2020).
10. J. S. Ayres, Surviving COVID-19: A disease tolerance perspective. *Sci Adv* **6**, eabc1518 (2020).
11. T. Narasaraju *et al.*, Excessive neutrophils and neutrophil extracellular traps contribute to acute lung injury of influenza pneumonitis. *Am J Pathol* **179**, 199-210 (2011).
12. K. L. Lin, Y. Suzuki, H. Nakano, E. Ramsburg, M. D. Gunn, CCR2+ monocyte-derived dendritic cells and exudate macrophages produce influenza-induced pulmonary immune pathology and mortality. *J Immunol* **180**, 2562-2572 (2008).
13. J. R. Aldridge, Jr. *et al.*, TNF/iNOS-producing dendritic cells are the necessary evil of lethal influenza virus infection. *Proceedings of the National Academy of Sciences of the United States of America* **106**, 5306-5311 (2009).
14. S. Herold *et al.*, Lung epithelial apoptosis in influenza virus pneumonia: the role of macrophage-expressed TNF-related apoptosis-inducing ligand. *J Exp Med* **205**, 3065-3077 (2008).
15. T. C. Dawson, M. A. Beck, W. A. Kuziel, F. Henderson, N. Maeda, Contrasting effects of CCR5 and CCR2 deficiency in the pulmonary inflammatory response to influenza A virus. *Am J Pathol* **156**, 1951-1959 (2000).
16. E. Pernet, J. Downey, D. C. Vinh, W. S. Powell, M. Divangahi, Leukotriene B4-type I interferon axis regulates macrophage-mediated disease tolerance to influenza infection. *Nat Microbiol* **4**, 1389-1400 (2019).
17. D. Talmi-Frank *et al.*, Extracellular Matrix Proteolysis by MT1-MMP Contributes to Influenza-Related Tissue Damage and Mortality. *Cell Host Microbe* **20**, 458-470 (2016).
18. L. E. Carlin, E. A. Hemann, Z. R. Zacharias, J. W. Heusel, K. L. Legge, Natural Killer Cell Recruitment to the Lung During Influenza A Virus Infection Is Dependent on CXCR3, CCR5, and Virus Exposure Dose. *Frontiers in Immunology* **9**, (2018).
19. E. Vivier, E. Tomasello, M. Baratin, T. Walzer, S. Ugolini, Functions of natural killer cells. *Nat Immunol* **9**, 503-510 (2008).

851 20. A. Glasner *et al.*, Elucidating the mechanisms of influenza virus recognition by Ncr1. *PLoS One* **7**,
852   e36837 (2012).
853 21. O. Mandelboim *et al.*, Recognition of haemagglutinins on virus-infected cells by NKp46 activates
854   lysis by human NK cells. *Nature* **409**, 1055-1060 (2001).
855 22. T. Li *et al.*, Respiratory Influenza Virus Infection Induces Memory-like Liver NK Cells in Mice. *J
856   Immunol* **198**, 1242-1252 (2017).
857 23. R. Gazit *et al.*, Lethal influenza infection in the absence of the natural killer cell receptor gene
858   Ncr1. *Nature Immunology* **7**, 517-523 (2006).
859 24. J. Stein-Streilein, J. Guffee, In vivo treatment of mice and hamsters with antibodies to asialo GM1
860   increases morbidity and mortality to pulmonary influenza infection. *J Immunol* **136**, 1435-1441
861   (1986).
862 25. J. P. McAleer, J. K. Kolls, Directing traffic: IL-17 and IL-22 coordinate pulmonary immune defense.
863   *Immunol Rev* **260**, 129-144 (2014).
864 26. S. Ivanov *et al.*, Interleukin-22 Reduces Lung Inflammation during Influenza A Virus Infection and
865   Protects against Secondary Bacterial Infection. *Journal of virology* **87**, 6911-6924 (2013).
866 27. C. Paget *et al.*, Interleukin-22 Is Produced by Invariant Natural Killer T Lymphocytes during
867   Influenza A Virus Infection POTENTIAL ROLE IN PROTECTION AGAINST LUNG EPITHELIAL
868   DAMAGES. *Journal of Biological Chemistry* **287**, 8816-8829 (2012).
869 28. H. L. Guo, D. J. Topham, Interleukin-22 (IL-22) Production by Pulmonary Natural Killer Cells and
870   the Potential Role of IL-22 during Primary Influenza Virus Infection. *Journal of virology* **84**, 7750-
871   7759 (2010).
872 29. P. Kumar, M. S. Thakar, W. Ouyang, S. Malarkannan, IL-22 from conventional NK cells is epithelial
873   regenerative and inflammation protective during influenza infection. *Mucosal Immunology* **6**, 69-
874   82 (2013).
875 30. D. A. Pociask *et al.*, IL-22 Is Essential for Lung Epithelial Repair following Influenza Infection.
876   *American Journal of Pathology* **182**, 1286-1296 (2013).
877 31. C. P. Baines *et al.*, Loss of cyclophilin D reveals a critical role for mitochondrial permeability
878   transition in cell death. *Nature* **434**, 658-662 (2005).
879 32. T. Nakagawa *et al.*, Cyclophilin D-dependent mitochondrial permeability transition regulates some
880   necrotic but not apoptotic cell death. *Nature* **434**, 652-658 (2005).
881 33. X. Zhao *et al.*, Bcl-xL mediates RIPK3-dependent necrosis in M. tuberculosis-infected
882   macrophages. *Mucosal Immunol* **10**, 1553-1568 (2017).
883 34. J. Downey, E. Pernet, F. Coulombe, M. Divangahi, Dissecting host cell death programs in the
884   pathogenesis of influenza. *Microbes Infect* **20**, 560-569 (2018).
885 35. J. Jaworska *et al.*, NLRX1 prevents mitochondrial induced apoptosis and enhances macrophage
886   antiviral immunity by interacting with influenza virus PB1-F2 protein. *Proceedings of the National
887   Academy of Sciences of the United States of America* **111**, E2110-2119 (2014).
888 36. H. E. Ghoneim, P. G. Thomas, J. A. McCullers, Depletion of alveolar macrophages during influenza
889   infection facilitates bacterial superinfections. *J Immunol* **191**, 1250-1259 (2013).
890 37. L. Chiossone *et al.*, Maturation of mouse NK cells is a 4-stage developmental program. *Blood* **113**,
891   5488-5496 (2009).
892 38. K. L. O'Brien, D. K. Finlay, Immunometabolism and natural killer cell responses. *Nat Rev Immunol*
893   **19**, 282-290 (2019).
894 39. M. P. Soares, L. Teixeira, L. F. Moita, Disease tolerance and immunity in host protection against
895   infection. *Nat Rev Immunol* **17**, 83-96 (2017).
896 40. S. Sengupta *et al.*, Circadian control of lung inflammation in influenza infection. *Nat Commun* **10**,
897   4107 (2019).

898 41. R. Collin *et al.*, An Unbiased Linkage Approach Reveals That the p53 Pathway Is Coupled to NK Cell
899   Maturation. *J Immunol* **199**, 1490-1504 (2017).
900 42. B. Fu *et al.*, CD11b and CD27 reflect distinct population and functional specialization in human
901   natural killer cells. *Immunology* **133**, 350-359 (2011).
902 43. A. Crinier *et al.*, High-Dimensional Single-Cell Analysis Identifies Organ-Specific Signatures and
903   Conserved NK Cell Subsets in Humans and Mice. *Immunity* **49**, 971-986 e975 (2018).
904 44. E. L. Gautier *et al.*, Gene-expression profiles and transcriptional regulatory pathways that underlie
905   the identity and diversity of mouse tissue macrophages. *Nat Immunol* **13**, 1118-1128 (2012).
906 45. A. Liberzon *et al.*, The Molecular Signatures Database (MSigDB) hallmark gene set collection. *Cell
907   Syst* **1**, 417-425 (2015).
908 46. T. Zhang *et al.*, Fibronectin maintains survival of mouse natural killer (NK) cells via
909   CD11b/Src/beta-catenin pathway. *Blood* **114**, 4081-4088 (2009).
910 47. A. Marçais *et al.*, The metabolic checkpoint kinase mTOR is essential for IL-15 signaling during the
911   development and activation of NK cells. *Nat Immunol* **15**, 749-757 (2014).
912 48. C. Yang *et al.*, mTORC1 and mTORC2 differentially promote natural killer cell development. *Elife*
913   **7**, (2018).
914 49. G. A. Porter, Jr., G. Beutner, Cyclophilin D, Somehow a Master Regulator of Mitochondrial
915   Function. *Biomolecules* **8**, (2018).
916 50. M. P. Longhi, A. Williams, M. Wise, B. P. Morgan, A. Gallimore, CD59a deficiency exacerbates
917   influenza-induced lung inflammation through complement-dependent and -independent
918   mechanisms. *European journal of immunology* **37**, 1266-1274 (2007).
919 51. M. J. van Helden, D. M. Zaiss, A. J. Sijts, CCR2 defines a distinct population of NK cells and mediates
920   their migration during influenza virus infection in mice. *PLoS One* **7**, e52027 (2012).
921 52. H. Peng *et al.*, Liver-resident NK cells confer adaptive immunity in skin-contact inflammation. *The
922   Journal of Clinical Investigation* **123**, 1444-1456 (2013).
923 53. D. K. Sojka *et al.*, Tissue-resident natural killer (NK) cells are cell lineages distinct from thymic and
924   conventional splenic NK cells. *Elife* **3**, e01659 (2014).
925 54. A. M. Abel, C. Yang, M. S. Thakar, S. Malarkannan, Natural Killer Cells: Development, Maturation,
926   and Clinical Utilization. *Frontiers in Immunology* **9**, (2018).
927 55. J. N. P. Smith *et al.*, Type I IFNs drive hematopoietic stem and progenitor cell collapse via impaired
928   proliferation and increased RIPK1-dependent cell death during shock-like ehrlichial infection. *PLoS
929   Pathog* **14**, e1007234 (2018).
930 56. M. Yamashita, E. Passegue, TNF-alpha Coordinates Hematopoietic Stem Cell Survival and Myeloid
931   Regeneration. *Cell Stem Cell* **25**, 357-372 e357 (2019).
932 57. C. A. Brady, L. D. Attardi, p53 at a glance. *J Cell Sci* **123**, 2527-2532 (2010).
933 58. A. V. Vaseva *et al.*, p53 opens the mitochondrial permeability transition pore to trigger necrosis.
934   *Cell* **149**, 1536-1548 (2012).
935 59. A. Bigi *et al.*, Cyclophilin D counteracts P53-mediated growth arrest and promotes Ras
936   tumorigenesis. *Oncogene* **35**, 5132-5143 (2016).
937 60. J. I. Belle *et al.*, p53 mediates loss of hematopoietic stem cell function and lymphopenia in Mysm1
938   deficiency. *Blood* **125**, 2344-2348 (2015).
939 61. S. M. Mendrysa *et al.*, mdm2 Is critical for inhibition of p53 during lymphopoiesis and the response
940   to ionizing irradiation. *Mol Cell Biol* **23**, 462-472 (2003).
941 62. S. Stegemann-Koniszewski *et al.*, Respiratory Influenza A Virus Infection Triggers Local and
942   Systemic Natural Killer Cell Activation via Toll-Like Receptor 7. *Front Immunol* **9**, 245 (2018).
943 63. B. R. Long *et al.*, Elevated Frequency of Gamma Interferon-Producing NK Cells in Healthy Adults
944   Vaccinated against Influenza Virus. *Clinical and Vaccine Immunology* **15**, 120-130 (2008).

945 64. I. D. Weiss *et al.*, IFN-gamma Treatment at Early Stages of Influenza Virus Infection Protects Mice
946   from Death in a NK Cell-Dependent Manner. *J Interf Cytok Res* **30**, 439-449 (2010).
947 65. D. Califano *et al.*, IFN-gamma increases susceptibility to influenza A infection through suppression
948   of group II innate lymphoid cells. *Mucosal Immunology* **11**, 209-219 (2018).
949 66. M. B. Graham *et al.*, Response to influenza infection in mice with a targeted disruption in the
950   interferon gamma gene. *J Exp Med* **178**, 1725-1732 (1993).
951 67. A. Iwasaki, E. F. Foxman, R. D. Molony, Early local immune defences in the respiratory tract. *Nat
952   Rev Immunol* **17**, 7-20 (2017).
953 68. F. Krammer *et al.*, Influenza. *Nat Rev Dis Primers* **4**, 3 (2018).
954 69. P. X. Kover, B. A. Schaal, Genetic variation for disease resistance and tolerance among Arabidopsis
955   thaliana accessions. *Proceedings of the National Academy of Sciences of the United States of
956   America* **99**, 11270-11274 (2002).
957 70. M. Divangahi, Are tolerance and training required to end TB? *Nat Rev Immunol* **18**, 661-663
958   (2018).
959 71. I. L. King, Y. Li, Host–Parasite Interactions Promote Disease Tolerance to Intestinal Helminth
960   Infection. *Frontiers in Immunology* **9**, (2018).
961 72. F. Tzelepis *et al.*, Mitochondrial cyclophilin D regulates T cell metabolic responses and disease
962   tolerance to tuberculosis. *Sci Immunol* **3**, (2018).
963 73. S. A. Condotta *et al.*, Cyclophilin D Regulates Antiviral CD8(+) T Cell Survival in a Cell-Extrinsic
964   Manner. *Immunohorizons* **4**, 217-230 (2020).
965 74. S. M. Fayaz, Y. V. Raj, R. G. Krishnamurthy, CypD: The Key to the Death Door. *CNS Neurol Disord
966   Drug Targets* **14**, 654-663 (2015).
967 75. M. Forte *et al.*, Cyclophilin D inactivation protects axons in experimental autoimmune
968   encephalomyelitis, an animal model of multiple sclerosis. *Proceedings of the National Academy
969   of Sciences of the United States of America* **104**, 7558-7563 (2007).
970 76. A. P. West, G. S. Shadel, S. Ghosh, Mitochondria in innate immune responses. *Nat Rev Immunol*
971   **11**, 389-402 (2011).
972 77. D. Wu *et al.*, Type 1 Interferons Induce Changes in Core Metabolism that Are Critical for Immune
973   Function. *Immunity* **44**, 1325-1336 (2016).
974 78. M. Kanayama *et al.*, Skewing of the population balance of lymphoid and myeloid cells by secreted
975   and intracellular osteopontin. *Nat Immunol* **18**, 973-984 (2017).
976 79. N. Khan *et al.*, M. tuberculosis Reprograms Hematopoietic Stem Cells to Limit Myelopoiesis and
977   Impair Trained Immunity. *Cell* **183**, 752-770.e722 (2020).
978 80. M. G. Netea *et al.*, Defining trained immunity and its role in health and disease. *Nat Rev Immunol*,
979   (2020).
980 81. E. Kaufmann *et al.*, BCG Educates Hematopoietic Stem Cells to Generate Protective Innate
981   Immunity against Tuberculosis. *Cell* **172**, 176-190 e119 (2018).
982 82. J. Kleinnijenhuis *et al.*, BCG-induced trained immunity in NK cells: Role for non-specific protection
983   to infection. *Clin Immunol* **155**, 213-219 (2014).
984 83. F. Coulombe *et al.*, Targeted prostaglandin E2 inhibition enhances antiviral immunity through
985   induction of type I interferon and apoptosis in macrophages. *Immunity* **40**, 554-568 (2014).
986 84. M. Z. Tay, C. M. Poh, L. Renia, P. A. MacAry, L. F. P. Ng, The trinity of COVID-19: immunity,
987   inflammation and intervention. *Nat Rev Immunol* **20**, 363-374 (2020).
988 85. W. K. E. Ip, N. Hoshi, D. S. Shouval, S. Snapper, R. Medzhitov, Anti-inflammatory effect of IL-10
989   mediated by metabolic reprogramming of macrophages. *Science* **356**, 513-519 (2017).
990 86. J. Schipke *et al.*, Assessment of cardiac fibrosis: a morphometric method comparison for collagen
991   quantification. *J Appl Physiol* **122**, 1019-1030 (2017).

992   87.   M. Martin, Cutadapt removes adapter sequences from high-throughput sequencing reads. *2011*
993   **17**, 3 (2011).
994   88.   N. L. Bray, H. Pimentel, P. Melsted, L. Pachter, Near-optimal probabilistic RNA-seq quantification.
995   *Nat Biotechnol* **34**, 525-527 (2016).
996   89.   C. Soneson, M. I. Love, M. D. Robinson, Differential analyses for RNA-seq: transcript-level
997   estimates improve gene-level inferences. *F1000Res* **4**, 1521 (2015).
998   90.   M. D. Robinson, D. J. McCarthy, G. K. Smyth, edgeR: a Bioconductor package for differential
999   expression analysis of digital gene expression data. *Bioinformatics* **26**, 139-140 (2010).
1000 91.   M. E. Ritchie *et al.*, limma powers differential expression analyses for RNA-sequencing and
1001   microarray studies. *Nucleic Acids Res* **43**, e47 (2015).
1002 92.   J. D. Storey, R. Tibshirani, Statistical significance for genomewide studies. *Proceedings of the*
1003   *National Academy of Sciences of the United States of America* **100**, 9440-9445 (2003).
1004 93.   Y. Nedelec *et al.*, Genetic Ancestry and Natural Selection Drive Population Differences in Immune
1005   Responses to Pathogens. *Cell* **167**, 657-669 e621 (2016).
1006 94.   G. Korotkevich, V. Sukhov, A. Sergushichev, Fast gene set enrichment analysis. *bioRxiv*, 060012
1007   (2019).
1008 95.   G. Bindea *et al.*, ClueGO: a Cytoscape plug-in to decipher functionally grouped gene ontology and
1009   pathway annotation networks. *Bioinformatics* **25**, 1091-1093 (2009).
1010 96.   A. Subramanian *et al.*, Gene set enrichment analysis: a knowledge-based approach for
1011   interpreting genome-wide expression profiles. *Proceedings of the National Academy of Sciences*
1012   *of the United States of America* **102**, 15545-15550 (2005).
1013 97.   P. Shannon *et al.*, Cytoscape: a software environment for integrated models of biomolecular
1014   interaction networks. *Genome Res* **13**, 2498-2504 (2003).
1015 98.   H. Yanai *et al.*, Tissue repair genes: the TiRe database and its implication for skin wound healing.
1016   *Oncotarget* **7**, 21145-21155 (2016).

1017

1018

1019   **AUTHOR CONTRIBUTIONS**

1020   M.D. conceived and supervised the project. J.D. and M.D. designed the experiments; J.D., E.P.

1021   and K.A.T performed experiments. Data were analyzed and interpreted by J.D. and M.D, except

1022   for RNA-seq data which were all analyzed and interpreted by H.E.R, under the supervision of

1023   L.B.B.. I.L.K. and S.A.K provided technical input/reagents, expertise and critically reviewed the

1024   manuscript. J.D., H.E.R., L.B.B and M.D. wrote the manuscript.

1025

1026   **DECLARATION OF INTEREST**

1027   The authors declare there are no competing interests.

1028

1029   **DATA AND MATERIALS AVAILABILITY**

1030   All raw data generated for this paper are available at GEO GSE163290, and processed data files

1031   are accessible on Zenodo (doi: 10.5281/zenodo.4300712). All code used for analysis, along with

1032   associated documentation, is available at https://github.com/herandolph/CypD_flu.

1033

1034   **ACKNOWLEDGEMENTS**

1048   **FIGURE LEGENDS**

1049   **Figure 1: CypD protects against IAV infection by promoting disease tolerance.** (A-B) WT

1050   and *CypD$^{-/-}$* mice were infected with the LD$_{50}$ dose of 90 PFU and survival (A) and weight loss

1051   (B) were monitored. (C-N) WT and *CypD$^{-/-}$* mice were infected with a sublethal dose of 50 PFU.

1052   At various time points post-infection viral load (C), total active IFN-I in the lungs (D) or BAL (E)

1053   were measured. (F) Lung wet-to-dry ratio at steady-state or at day 7 post-infection. Protein (G) or

1054   erythrocytes (H) in the BAL of mice at various timepoints post-infection. (I) Fluorescence intensity

1055   of lungs following one hour of Texas-Red Dextran administration. The left panels are

1056   representative lung images from two separate experiments and are quantified on the right. Total

1057   cell counts in the lungs (J) and BAL (K) following infection. Representative micrographs of lungs

1058   stained with hematoxylin and eosin (L; scale bar = 30 μM) or Masson's Trichrome (M; scale bar

1059   = 20μM) that are either uninfected or infected for 7 days, as quantified in (N). In A and B, total

1060   mice are denoted in the figures, in C-K each symbol represents a unique mouse, in L and M

1061   micrographs are representative of at least 5 mice and in N each symbol represents the

1062   quantification of one random micrograph (n=10 micrographs total). All figures are a compilation

1063   of at least two experiments. Statistical analyses were performed using the Log Rank Test (A),

1064   Two-way ANOVA followed by Sidak's multiple comparison test (B-H, J-K, N) or Two-tailed

1065   Student's T-Test (I). See also **Figure S1**.

1066

1067   **Figure 2: CypD mediates disease tolerance via hematopoietic cells and mice exhibit altered**

1068   **NK cell responses upon infection.** (A-J) Mice were infected with 50 PFU of IAV. (A-D) Chimeric

1069   mice were generated by reconstituting irradiated CypD-deficient mice (CD45.2) with WT CD45.1

1070   bone marrow (WT → *CypD$^{-/-}$*) or irradiated CD45.1 mice with CypD-deficient (CD45.2) bone

44

1071   marrow ($CypD^{-/-} \rightarrow$ WT). Chimeric mice were infected for 7 days and total erythrocytes in the

1072   BAL (A) were quantified. Representative micrographs of hematoxylin and eosin-stained lungs (B;

1073   scale bar = 30 μM) or Masson's Trichrome (C; scale bar = 30 μM) as quantified in (D). (E-G)

1074   BAL from WT and $CypD^{-/-}$ mice were phenotyped by flow cytometry and total frequencies (left

1075   panels) and total cell counts (right panels) of IMM (E), neutrophils (F) and NK cells (G)

1076   enumerated. Mean fluorescence intensities of perforin and granzyme B of NK cells at day 7 (H)

1077   post-IAV infection. (I) Representative FACS plot of CD27 and CD11b expression on NK cells in

1078   the BAL of WT versus CypD-deficient mice at 7 days post-infection. (J) Quantifications of the

1079   percentages (left panel) and total cells counts (right panel) of NK cell activation subsets in the

1080   BAL at day 7 post-infection. In each panel, each symbol indicates a separate mouse, except in B-

1081   C, which is a representative figure of 4 mice/group, D, where each symbol is a randomly quantified

1082   micrograph (n=10 micrographs) and I, which is a representative plot compiled in J. All figures are

1083   a compilation of at least two experiments, except for H, which is one representative experiment of

1084   two. Statistical analyses were performed using the One-way ANOVA followed by Tukey's

1085   multiple comparisons (A, D), Two-way ANOVA followed by Sidak's multiple comparison test

1086   (E-G, J) or Two-tailed Student's T-Test (H). See also **Figure S2**.

1087

1088   **Figure 3: $CypD^{-/-}$ alters the transcriptome of IAV-infected splenic NK cells and induces a**

1089   **distinct metabolic phenotype.** (A) Volcano plot of genes significantly differentially expressed

1090   (DE) between IAV-infected splenic NK cells of WT (blue, log2 fold change (FC) < -0.5, FDR <

1091   0.10) and $CypD^{-/-}$ (green, log2 FC > 0.5, FDR < 0.10) mice. Genes with a negative log2 FC show

1092   higher expression in WT mice, while genes with a positive log2 FC show higher expression in

1093 $CypD^{-/-}$ mice. Selected genes show the most extreme changes in expression between the two

1094   genotype groups. (B) Significant (FDR < 0.01) ClueGO pathway enrichments for genes showing

1095   higher expression (FDR < 0.10) in the WT mice versus (C) *CypD*$^{-/-}$ mice in IAV-infected splenic

1096   NK cells. (D) Heatmap showing expression levels (mean-centered and scaled) for a subset of

1097   maturity marker genes as identified in Chiossone et al. (*37*) in IAV-infected NK cells of WT and

1098   *CypD*$^{-/-}$ mice. ("imm" = immature NK [CD27+CD11b-], "int" = intermediate-mature NK

1099   [CD27+CD11b+], "mature" = mature NK [CD27-CD11b+]). (E) Barcode enrichment plots for the

1100   hallmark Wnt/β-catenin signaling, (F) mTORC1 signaling and (G) oxidative phosphorylation

1101   pathways. A positive enrichment score (ES) corresponds to pathway enrichment among genes

1102   more highly expressed in *CypD*$^{-/-}$ mice (green), while a negative ES corresponds to pathway

1103   enrichment among genes more highly expressed in WT mice (blue). (H) Average, scaled logCPM

1104   expression estimates across genes in the hallmark Wnt/β-catenin signaling pathway. Oxygen

1105   consumption on purified splenic NK cells at day 3 (I-L) or day 5 (M-P) post-infection. (I, M)

1106   Representative Seahorse curves from which the values in (J-L) and (N-P) were calculated,

1107   respectively. (Q) Representative flow cytometry plots of splenic NK cells differentially stained for

1108   Mitotracker Orange and Mitotracker Green, as quantified in (R-S). Healthy respiring mitochondria

1109   were considered as Orange^{hi} and Green^{hi} (R) and disrupted mitochondria were considered as

1110   Orange^{lo} and Green^{hi} (S). (T) Frequency of MitoSox Red^{hi} NK cells in the spleen. (I-P) All data

1111   are from one representative experiment of two independent experiments and each dot is indicative

1112   of a technical replicate of NK cells compiled from 5 different mice. (Q-T) Data are compiled from

1113   two independent experiments and each dot represents a unique mouse. Statistical differences were

1114   assessed by Student's T-Test (J-L and N-P) or Two-way ANOVA followed by Sidak's multiple

1115   comparisons test (R-T). See also **Figure S3**.

1116

1117

1118   **Figure 4: Splenic NK cells of *CypD⁻/⁻* mice are functionally reprogrammed.** (A) Heatmap

1119   showing expression levels (mean-centered and scaled) for selected subsets of genes that fall into

1120   ontology pathways and functional gene sets significantly enriched among WT or (B) *CypD⁻/⁻* gene

1121   sets in IAV-infected splenic NK cells. (C) Proportion of WT or *CypD⁻/⁻* differentially-expressed

1122   genes that are in the tissue repair (TiRe) dataset (*98*) (WT, blue dashed line, p = 0.009; *CypD⁻/⁻*,

1123   green dashed line, p = 0.798) compared to random expectation when sampling the same total

1124   number of WT or *CypD⁻/⁻* differentially-expressed genes 1,000 times from all genes tested (null,

1125   density distributions).

1126

1127   **Figure 5: CypD-deficient mice have impaired recruitment of activated NK cells from the**

1128   **peripheral blood.** (A-G) WT and *CypD⁻/⁻* were infected with 50 PFU. (A) Intracellular expression

1129   of Ki67, indicative of proliferative cells, in NK cells of the BAL. Left panels show a representative

1130   FACS plot as quantified on the right at day 5 post-infection. (B) Intracellular expression of active

1131   Caspase 3 expression by flow cytometry, indicative of apoptotic NK cells in the BAL of infected

1132   mice. The panels on the left are of a representative FACS plot at day 5 post-infection, as quantified

1133   on the right. (C) CCR2 expression on NK cells of the BAL with a day 5 representative FACS plot

1134   on the left and quantified on the right. (D) Differential expression of CD49b versus CD49a on NK

1135   cells of the BAL with a representative FACS plot on the left. (E-F) At various times post-infection

1136   peripheral blood was collected and the frequency of NK cells (E) and their activation state as

1137   defined by CD27 and CD11b expression (F-G) were quantified. In the left panel of F is a

1138   representative FACS plot of NK cells at day 5 post-infection. Each panel represents the

1139   compilation of at least two experiments, except C which is one representative experiment of two

1140 independent experiments. Each symbol represents one unique mouse. For all panels, Two-way

1141 ANOVA followed by Sidak's multiple comparisons test was performed to determine significance.

1142 See also **Figure S4**.

1143

1144 **Figure 6: *CypD$^{-/-}$* mice have reduced NK cell hematopoiesis in the bone marrow of infected**

1145 **mice due to cell death of progenitors.** (A) Schematic of NK cell hematopoiesis starting at

1146 pluripotent LKS cells down to NK cells. (B-G) Total cell counts of LKS (B), CLP (C), pre-NKP

1147 (D-E), NKP (D, F) and differential activation statuses of mature NK cells (G) as assessed by flow

1148 cytometry. (D) Representative FACS plots of pre-NKP and NKP populations in the bone marrow

1149 at 5 days post-infection. In B, C and G, left panels are representative FACS plots taken at day 3

1150 (B-C) and day 5 (G) post-infection. (H-I) Expression of p53 within pre-NKP (H) and NKP (I)

1151 populations in the bone marrow. Left panels are representative histograms taken at 5 days post-

1152 infection as quantified in the right panels. (J) Differential expression of AnnexinV and NucSpot to

1153 determine the levels of dead cells within the NKP population at various times post-infection. FACS

1154 plots on the left are taken from day 5 post-IAV infection. Panels in B-F and I-J are a compilation

1155 of at least 2 experiments, while G-H are one representative experiment of three independent

1156 experiments, with each symbol representing an individual mouse. In all panels, significance was

1157 assessed by Two-way ANOVA followed by Sidak's multiple comparisons test. See also **Figure**

1158 **S4**.

1159

1160 **Figure 7: Reduced IL-22 production by NK cells in the airways is responsible for the**

1161 **susceptibility of *CypD$^{-/-}$* mice.** (A) Levels of IFN-γ in the BAL of infected WT and *CypD$^{-/-}$* mice

1162 as determined by ELISA. (B) Intracellular cytokine staining of IFN-γ in NK cells. FACS plots are

48

1163   representative of the quantification on the right and are gated against the FMO. (C) Levels of IL-

1164   22 in the BAL of infected WT and *CypD$^{-/-}$* mice as determined by ELISA. (D) Intracellular

1165   cytokine staining for IL-22 by NK cells in the BAL. FACS plots on the left are representative of

1166   the quantification on the right. An IL-22-deficient mouse was used as a staining control for

1167   specificity. (E) Model of recombinant IL-22 experiments as used in F-I. (F) Mice were infected

1168   with LD$_{50}$ 90 PFU, administered recombinant IL-22 or PBS on day 5 p.i. and survival monitored.

1169   (G-I) a sublethal dosage of 50 PFU was used and mice were administered IL-22 or PBS as before.

1170   At day 7, viral loads were quantified (G), pulmonary inflammation and fibrosis were assessed by

1171   hematoxylin and eosin or Masson's Trichrome staining, respectively (H; scale bar = 30µM) or

1172   erythrocytes in the BAL were enumerated (I). (J) Schematic of NK cell transfer experiments

1173   performed in K-N. On day 7 post-infection, day 2 post-transfer, protein (L), erythrocyte (M) and

1174   leukocyte levels in the BAL or lung viral loads (N) were assessed. In panels A, C, F, I, K, L and

1175   N data are combinations of two or three independent experiments. In B, D, G and M data are from

1176   one experiment that is representative of two or three independent experiments. Micrographs in H

1177   are representative of 3 or 4 individual mice. In A-D, G, I and K-N, each symbol represents data

1178   from one individual mouse, while in H total n values are displayed in the panel legend. Statistical

1179   analyses were performed as follows: in A-D Two-way ANOVA followed by Sidak's multiple

1180   comparisons test; F Log Rank Test; G, I Two-way ANOVA followed by Tukey's multiple

1181   comparisons test; K-N One-way ANOVA followed by Dunnett's multiple comparisons test,

1182   Kruskal-Wallis test. See also **Figure S5**.

1183

1184

1185

1186   **SUPPLEMENTARY FIGURE LEGENDS:**

1187   **Supplementary Figure 1: Susceptibility of CypD-deficient is due to disease tolerance and not**

1188   **host resistance mechanisms.** (A-D) Mice were infected with 50 PFU of IAV and levels of LDH

1189   in the BAL (A), IFN-β in the lung (B) or BAL (C) were quantified. (D) Representative pictures of

1190   the BAL of mice over the course of infection as quantified in **Figure 1H**. Gating strategy for WT

1191   (E) and *CypD$^{-/-}$* (F) mice used to quantify innate cells in the study. In panels A-C, each symbol

1192   indicates a separate mouse. Panel A is a compilation of two independent experiments and B-C are

1193   from one experiment. In panels A-C differences were assessed by Two-way ANOVA followed by

1194   Sidak's multiple comparisons test. Refers to **Figures 1-2**

1195

1196   **Supplementary Figure 2: Kinetics and activation of NK cells**. (A) Representative flow

1197   cytometry plots validating reconstitution of chimeric mice. (B-H) Mice were infected with 50 PFU

1198   of IAV. (B) Total cell counts in the BAL of chimeric mice at 7 days post-infection. (C-E)

1199   Frequencies (left panels) and total cell counts (right panels) of (IMM) (C), neutrophils (D) and NK

1200   cells (E) in the lung. (F) Representative FACS plots of NK cell activation in the lung at day 7 and

1201   quantified in (G) with frequencies in the left panel and total cell counts in the right. (H) Frequencies

1202   (left panels) and total cell counts (right panels) of NK cell activation in the spleen at day 5 post-

1203   IAV infection. In each panel, each symbol represents an individual mouse. Each panel is a

1204   compilation of two individual experiments, except H which is one representative experiment of

1205   two. Statistical differences were determined by One-way ANOVA followed by Dunnett's test in

1206   B, or Two-way ANOVA followed by Sidak's multiple comparisons test in all other panels. Refers

1207   to **Figure 2**.

1208

1209 **Supplementary Figure 3. RNA-sequencing of purified, splenic NK cells in control and IAV-**

1210 **infected conditions.** (A) Expression of *CypD* in purified NK cells by qPCR. (B) PCA

1211 decomposition of the splenic NK cell expression data in WT (blue) and *CypD$^{-/-}$* (green) mice in

1212 control and IAV-infected conditions. PC1 (percent variance explained = 56.3%) separates samples

1213 by infection status. (C) Barcode enrichment plots for maturity marker gene sets as defined in

1214 Chiossone et al. 2009. A negative enrichment score (ES) corresponds to pathway enrichment

1215 among genes more highly expressed in WT mice. (D) Average, scaled logCPM expression

1216 estimates across genes in the mTORC1 signaling pathway and (E) the oxidative phosphorylation

1217 pathway in IAV-infected splenic NK cells of WT and *CypD$^{-/-}$* mice. (F-I) Oxygen consumption of

1218 naïve purified splenic NK cells as detailed in Figure 3I-P. Statistical differences were assessed in

1219 G-I by Student's T-test. Refers to **Figure 3**.

1220

1221 **Supplementary Figure 4: Kinetics of recruited NK cells and NK cell hematopoiesis in the**

1222 **bone marrow of WT and *CypD$^{-/-}$* mice.** (A-E) Mice were infected with 50 PFU of IAV. The

1223 percentage of CCR2-expressing NK cells in the lung (A) and blood (B). (C) Differential expression

1224 of CD49b and CD49a in the lung, with a representative FACS plot on the left and quantified on

1225 the right. (D-E) Activation status of NK cells in the blood in uninfected (D; representative FACS

1226 plot on the left) and day 3 (E) post-infection. (F-O) Mice were infected with 50 PFU of IAV and

1227 phenotyped by flow cytometry. Frequencies of LKS (F) and CLPs (G) following infection were

1228 determined as well as frequencies (left panels) and total cell counts (right panels) of CMPs (H)

1229 and GMPs (I). Relative activation states of naïve NK cells in the BM (J), as well as the percentage

1230 (left panels) and total cell counts (right panels) of Ki67-expressing pre-NKPs (K) and NKPs (L).

1231 Level of expression of p53 in NK cells in the bone marrow (M) and BAL (N) at day 5 post-

51

1232   infection. (O) Representative FACS plot (left panel) and quantification (right panel) of cell death

1233   in pre-NKPs as determined by AnnexinV and NucSpot staining. Symbols indicate an individual

1234   mouse and B, D, F-I, K-L and O are compilations of two individual experiments and A, C, E, J,

1235   M-N are one representative experiment of two. Statistical differences were assessed by Two-way

1236   ANOVA followed by Sidak's multiple comparisons test for all panels, except for N where a Two-

1237   tailed Student's T-test was performed. Refers to **Figures 5 and 6.**

1238

1239   **Supplementary Figure 5: Disease tolerance is mediated by IL-22 and not IFN-γ following**

1240   **IAV infection.** (A-K) Mice were infected with 50 PFU of IAV. (A) The frequency of IFN-γ-

1241   producing splenic NK cells at day 5 post-infection. (B-D) WT and *Ifngr*$^{-/-}$ mice were infected and

1242   the levels of protein (B), erythrocytes (C) and total cells (D) in the BAL at 7 days post-infection

1243   were determined. Following administration of recombinant IFN-γ, levels of protein (E) and

1244   erythrocytes (F) were assessed in the BAL. (G-I) WT and IL-22-deficient mice were infected and

1245   amount of protein (G) and number of cells (H) were enumerated, as well as pulmonary

1246   inflammation by hematoxylin and eosin staining (I; scale bar = 30μM). (J) Frequency of IL-22-

1247   producing NK cells in the spleens of WT and CypD-deficient mice at 5 and 7 days post-IAV

1248   infection. In all panels except I and K, symbols represent an individual mouse. In I, micrographs

1249   are a representative image taken from one of four mice. In K quantification is done from 10 random

1250   micrographs and each symbol represents one micrograph. In A and J, data are taken from one

1251   experiment that is representative of three. In B-H, panels are a compilation of two individual

1252   experiments. Differences were determined as follows: in A-D, G-H Two-tailed Student's T-test;

1253   in E, F, K Two-way ANOVA followed by Tukey's multiple comparisons test or Sidak's (J). Refers

1254   to **Figure 7**.

1255 **Supplementary Table 1: RNA-Seq sample meta-data**

1256 **Supplementary Table 2: CypD knockout effect on gene expression**

1257 **Supplementary Table 3: Gene set enrichment analysis in WT and *CypD^{-/-}* NK cells**
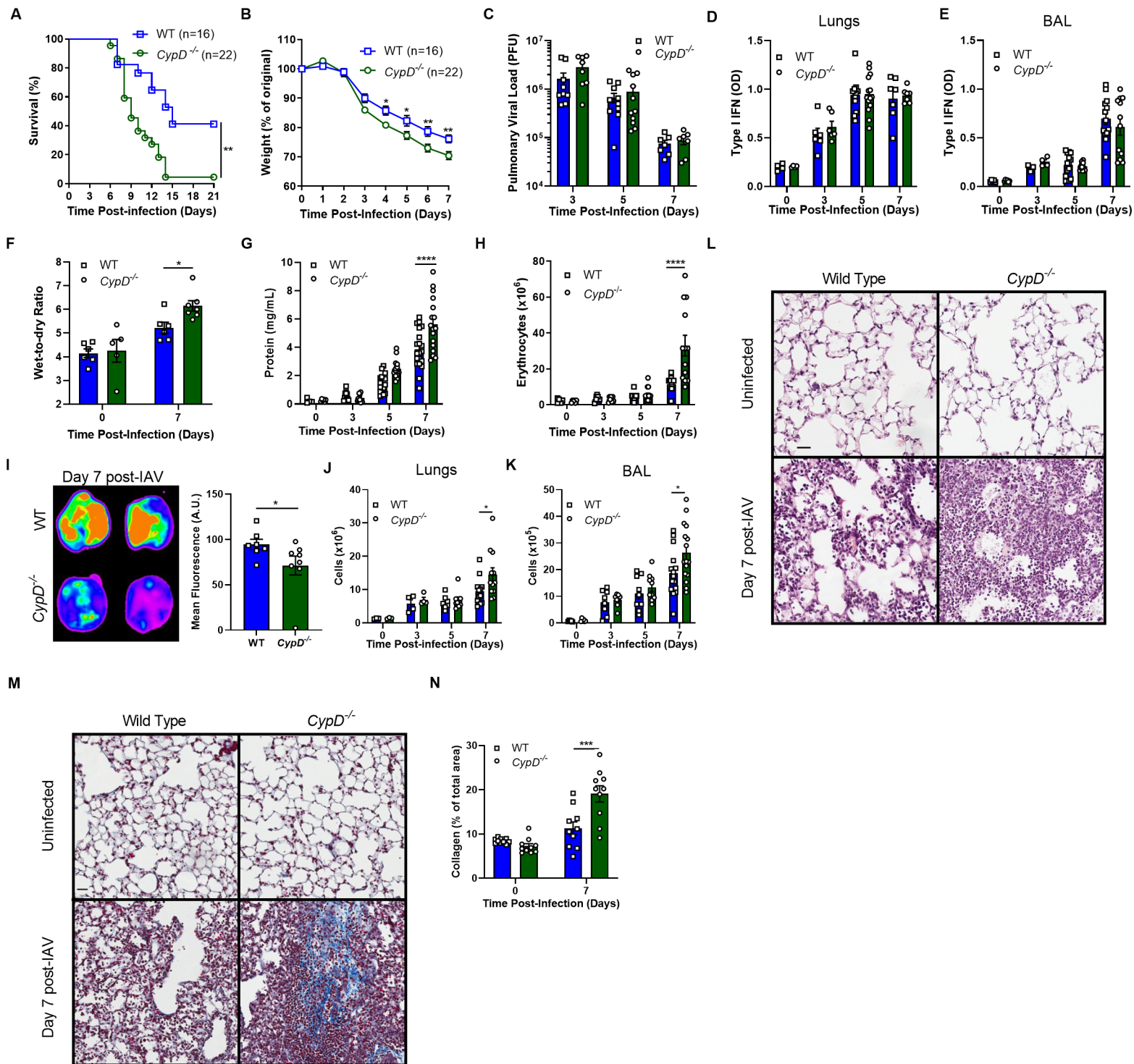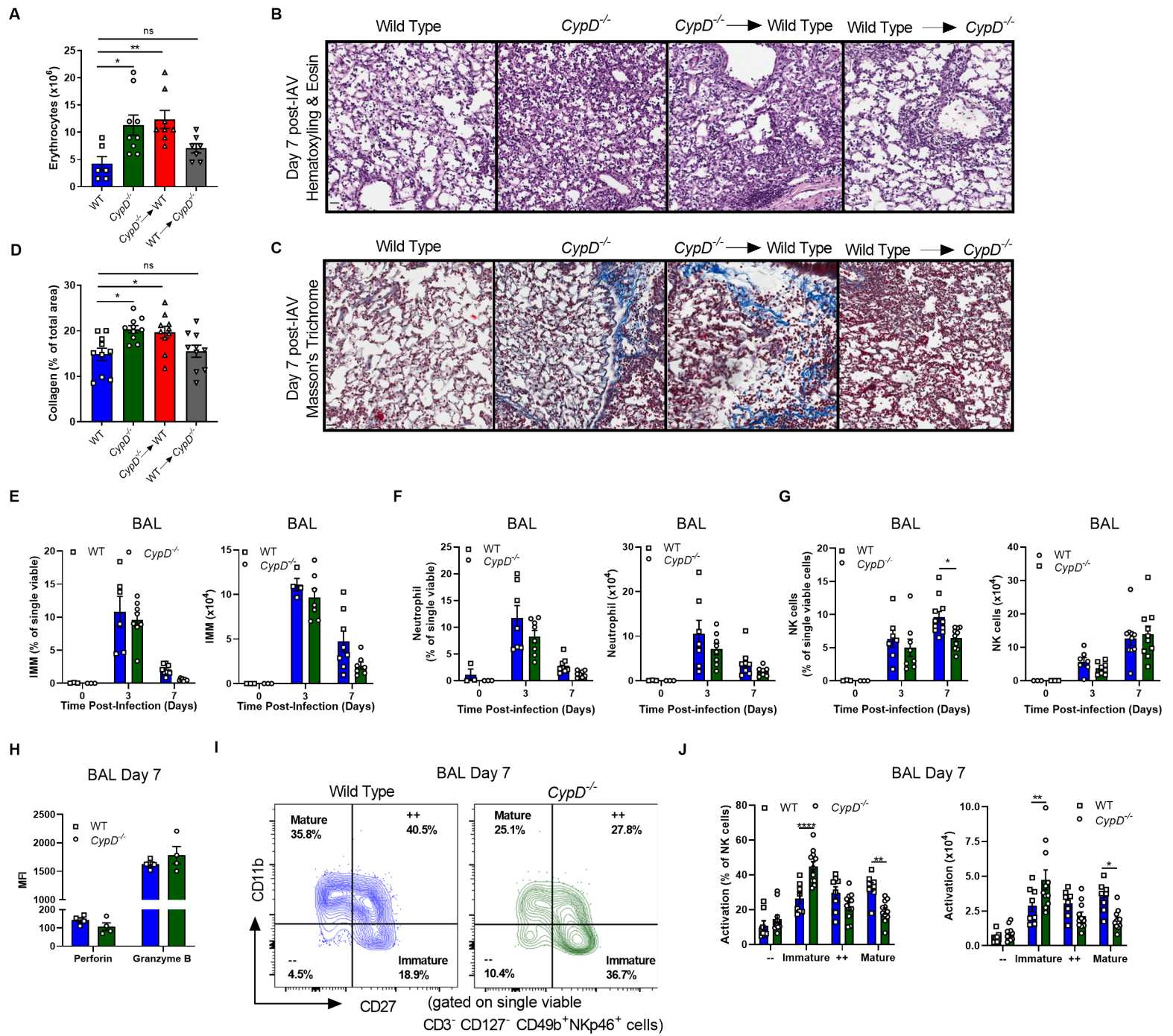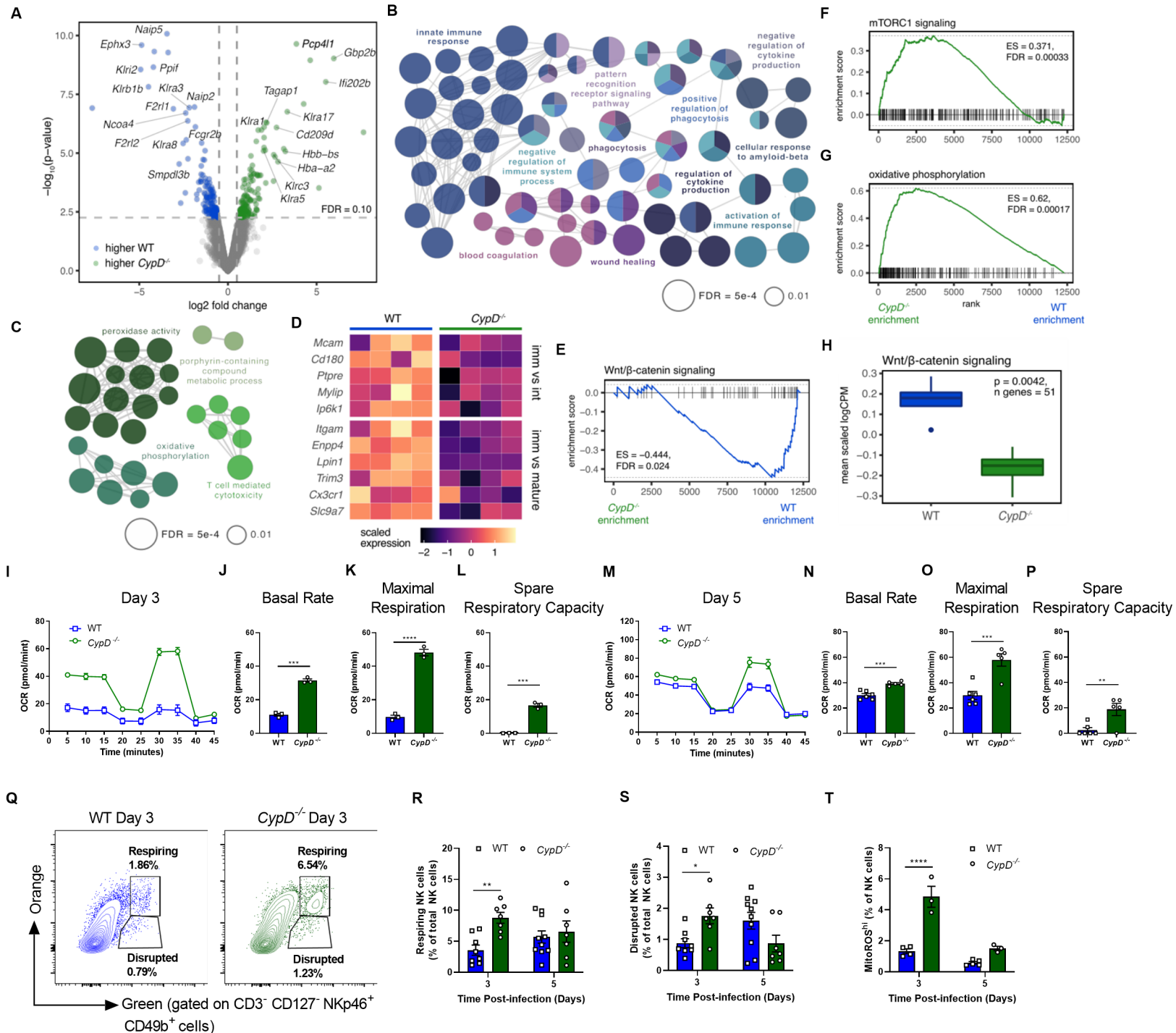
1258

FIGURE 1:

FIGURE 2:

FIGURE 3:
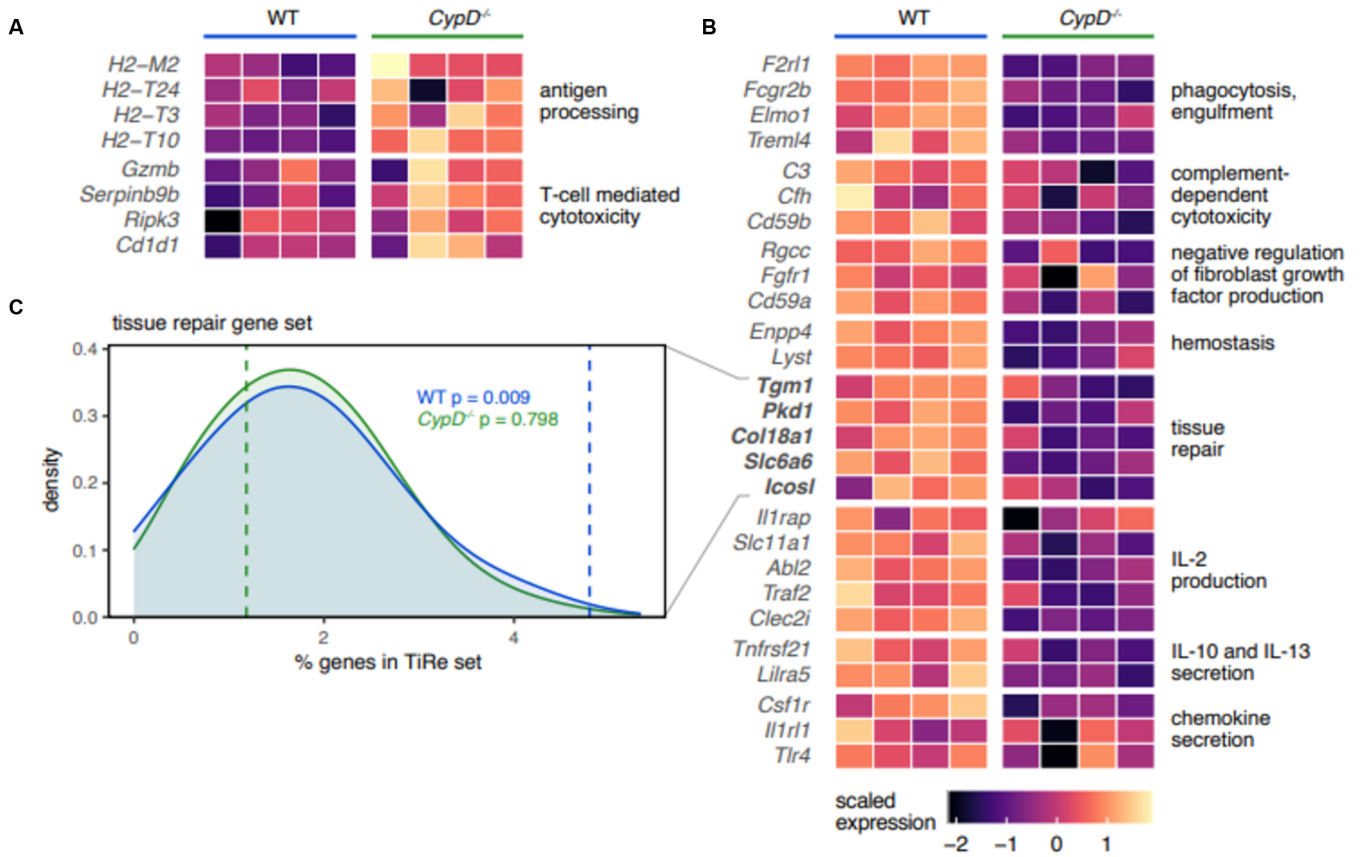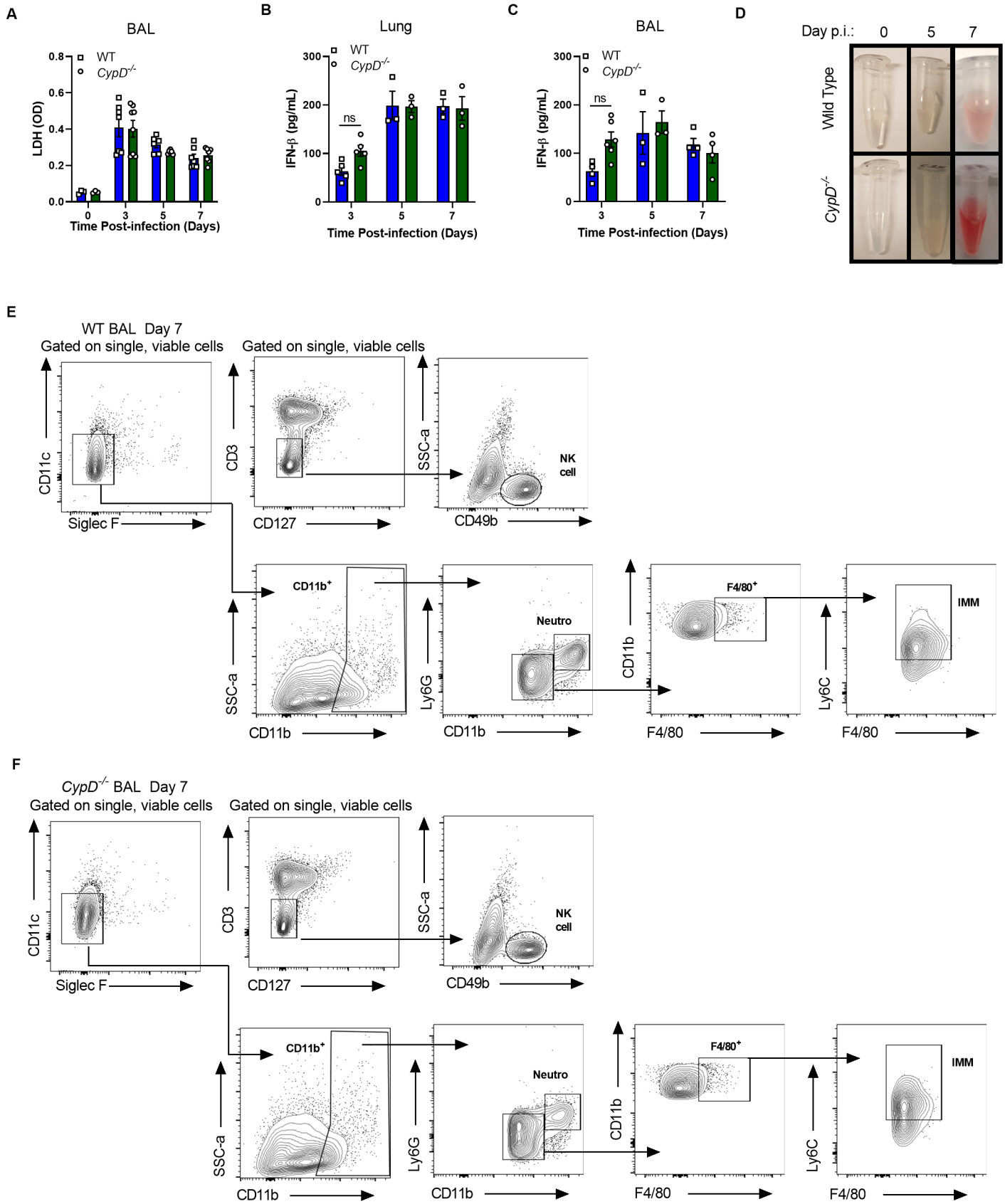
FIGURE 4:
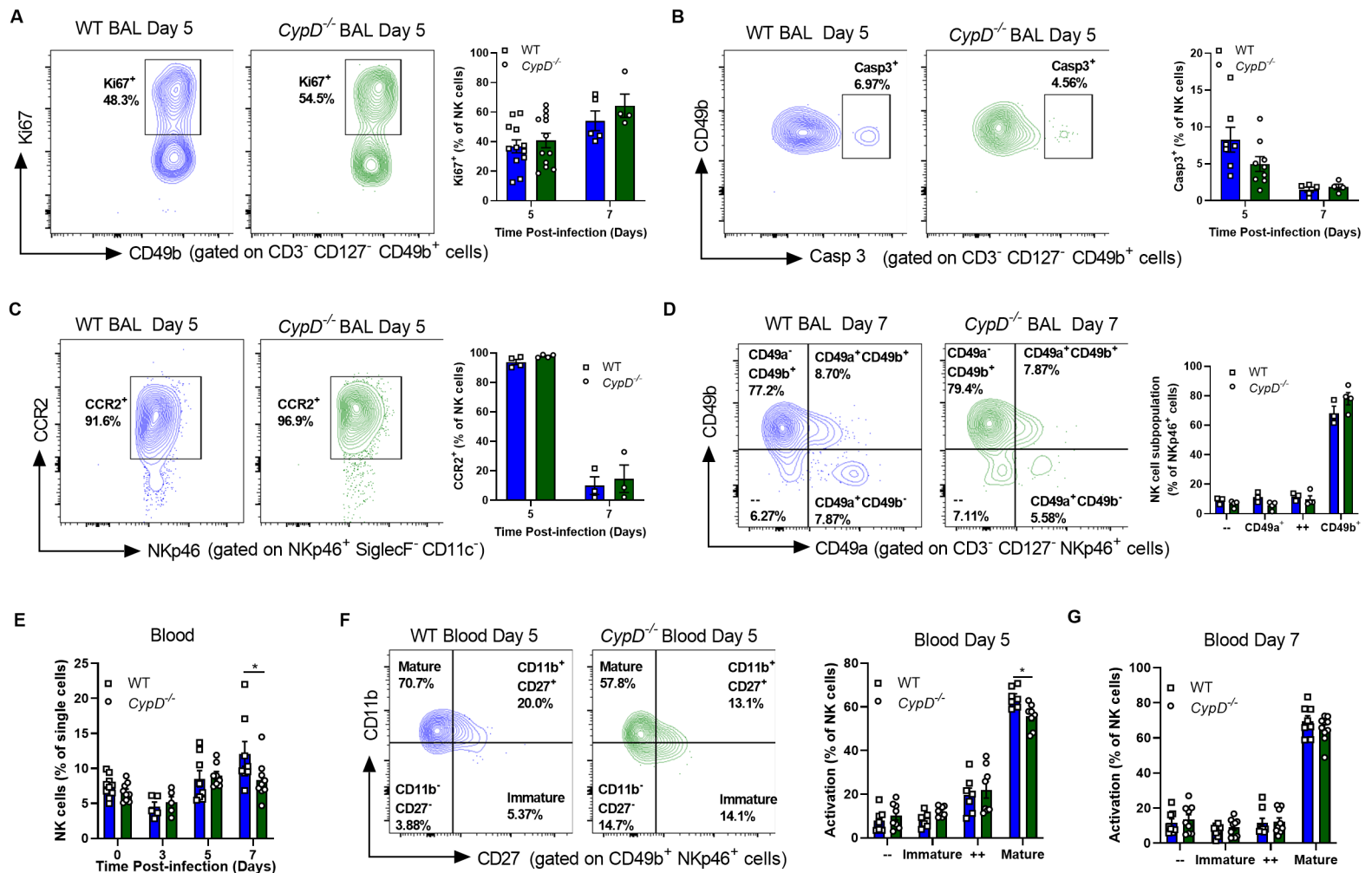
FIGURE 5:
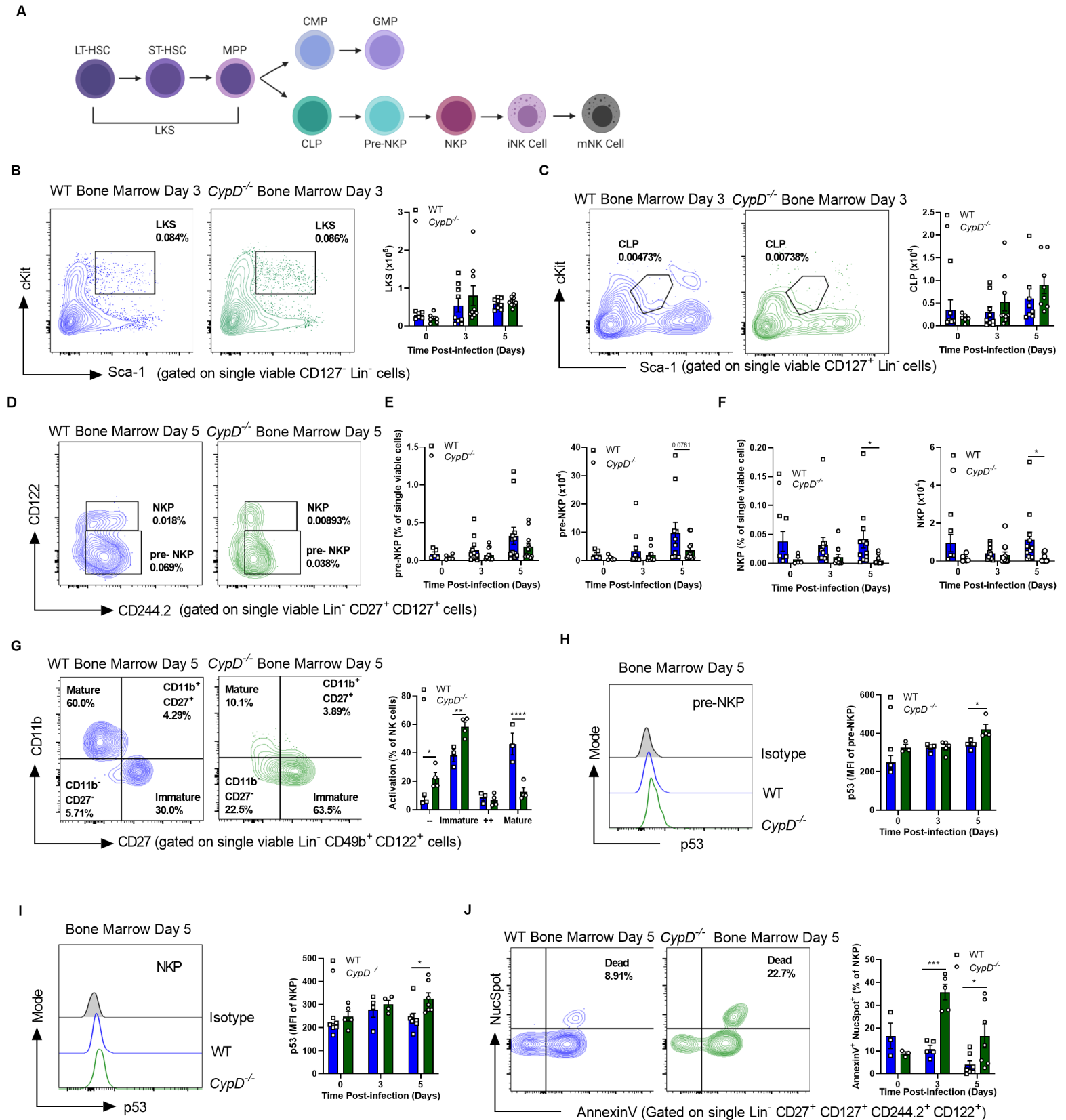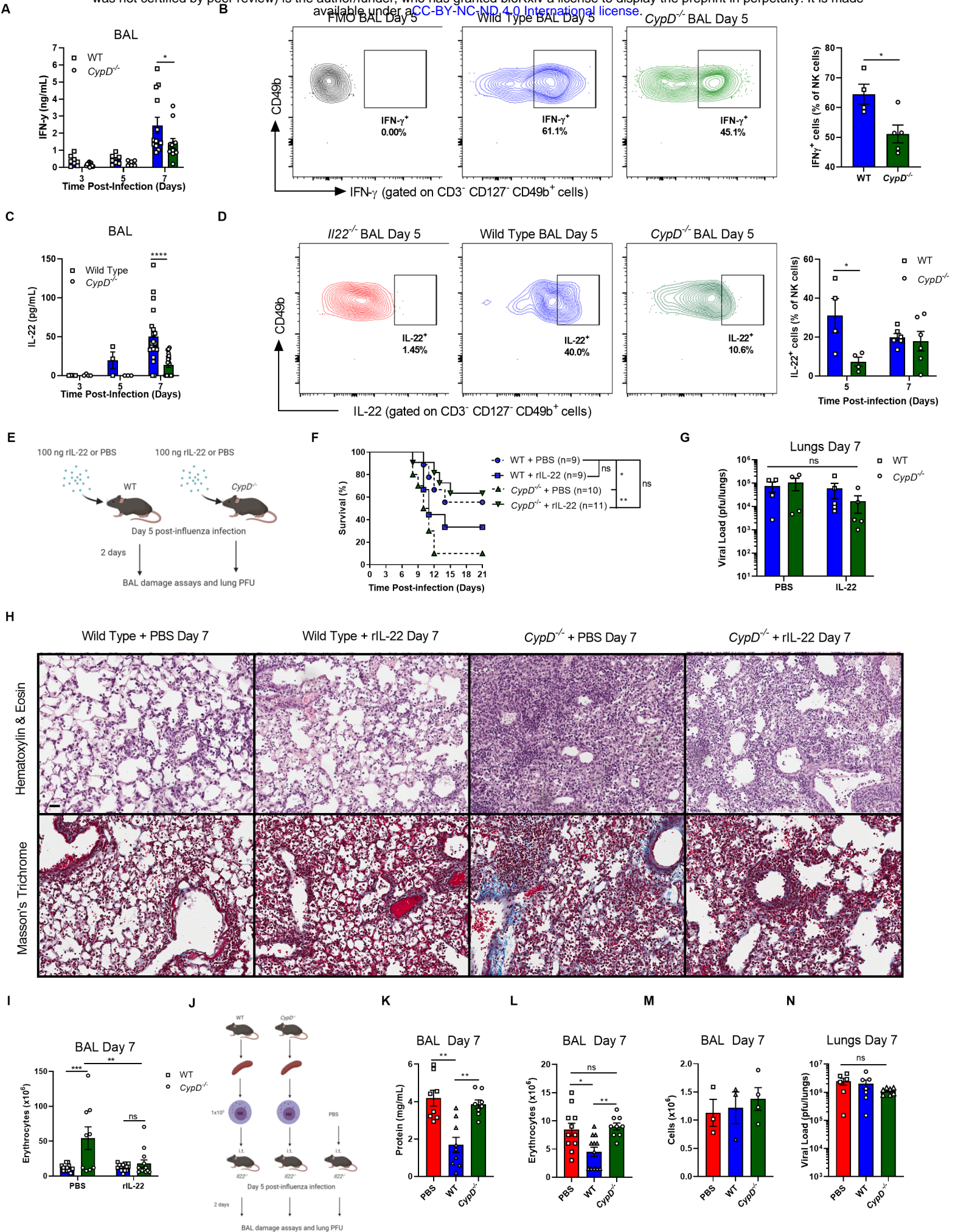
FIGURE 6:

FIGURE 7.

Figure S1

SUPPLEMENTARY FIGURE 2:
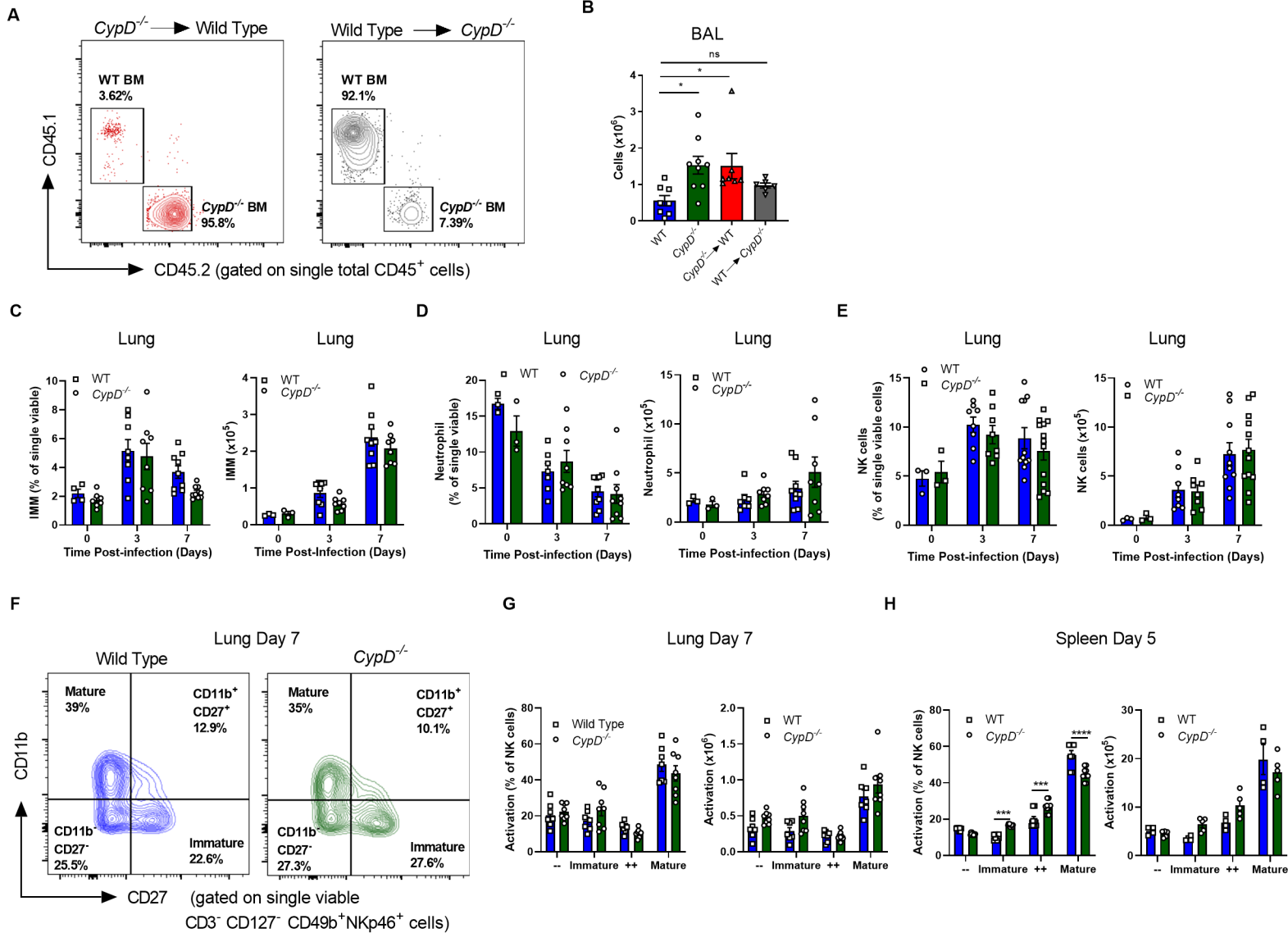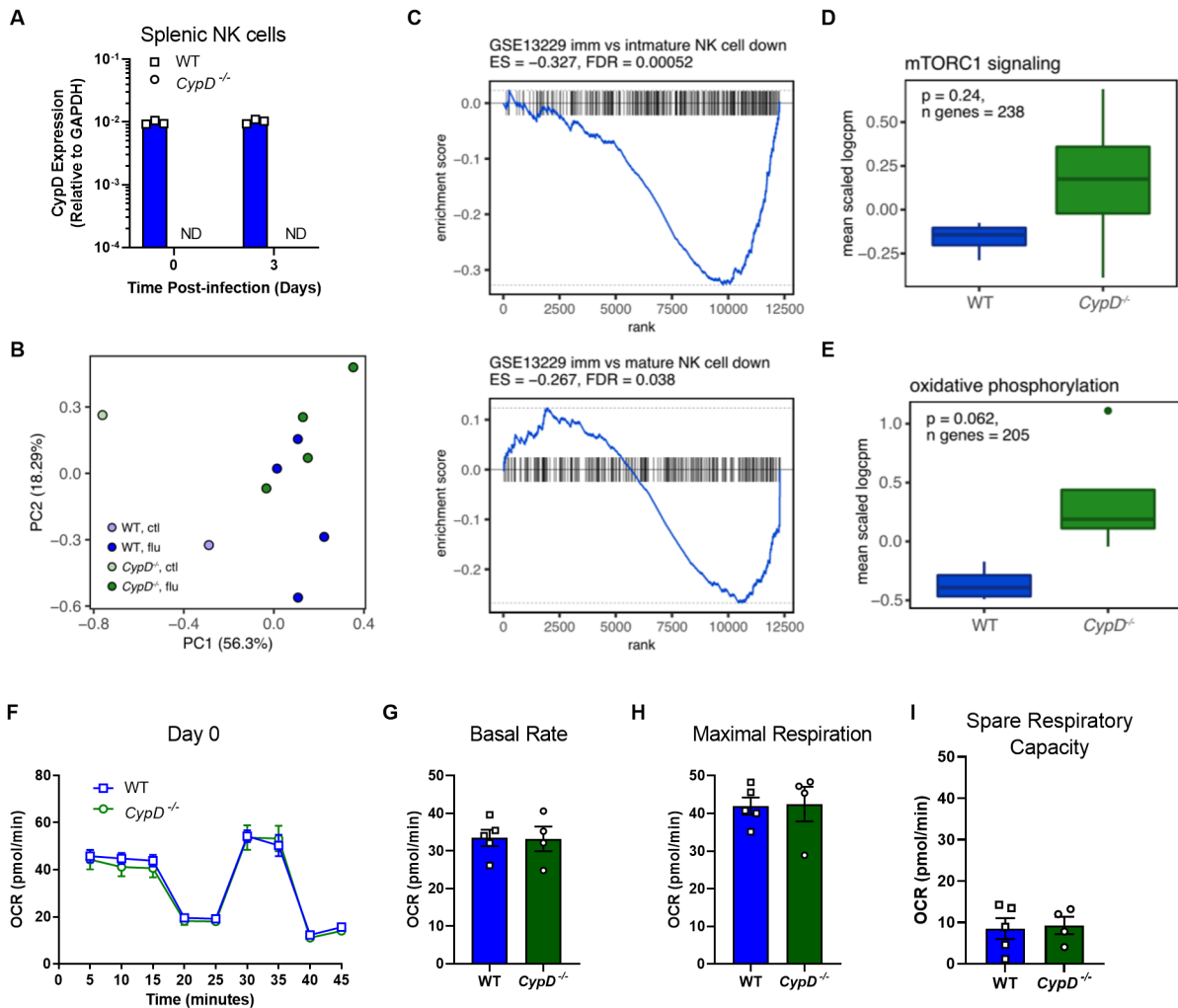
SUPPLEMENTARY FIGURE 4:

SUPPLEMENTARY FIGURE 5:

A Spleen Day 5

B BAL Day 7

C BAL Day 7

D BAL Day 7

E BAL Day 7

F BAL Day 7

G BAL Day 7

H BAL Day 7

I Wild Type Day 7 — $Il22^{-/-}$ Day 7

J Spleen

K